

Phase diagram of the quantum spin-1/2 Heisenberg- Γ model on a frustrated zigzag chain

Hidehiro Saito* and Chisa Hotta

Department of Basic Science, University of Tokyo, Meguro-ku, Tokyo 153-8902, Japan

(Dated: June 25, 2024)

We investigate the quantum spin-1/2 zigzag chain with frustrated J_1 - J_2 Heisenberg interactions, incorporating additional off-diagonal exchange interactions known as the Γ term, both with and without an applied magnetic field. Based on the density-matrix renormalization group calculation, we map out the ground state phase diagram that shows a variety of magnetic and nonmagnetic phases including multicritical points and several exactly solvable points. Upon introducing a finite Γ term, we observe the persistent dimer singlet state of the J_1 - J_2 Heisenberg model, sustaining a nonzero spin gap, while also giving rise to a gapless nonmagnetic excitation, manifesting in the substantial zero-energy peak in the nematic dynamical structure factor. This gapless peak-mode remaining almost as a fluctuation to the ground state, induces dilute but robust concentration of nematicity on top of singlets on dimers, which we call the nematic singlet-dimer phase. When the whole nematic excited mode condenses and replaces the singlet, the nematic-dimer phase transforms to the Ising-type ferromagnetic or antiferromagnetic long-range orders that arise from the Γ term spontaneously selecting magnetic easy axes. Its orientations dictate the type of magnetic order under geometric frustration effects as predicted by Landau's mean-field theory. These theoretical findings provide insights into the exotic low-temperature phase observed in YbCuS_2 , characterized by gapless excitations and seemingly nonmagnetic behavior accompanied by incommensurate correlations.

I. INTRODUCTION

Exploring interesting quantum-disordered phases in materials stands by now as a major challenge in condensed matter physics. Longstanding intense investigations into triangular and kagome quantum spin liquids¹⁻³ were recently spurred by the discovery of Kitaev spin liquids featuring Majorana quasiparticle excitations⁴, and it motivated the detailed examination of new types of quantum anisotropic exchange interactions in 4d, 5d, and 4f insulating magnets⁵⁻⁸. These interactions are influenced by strong spin-orbit coupling, moderate crystal field effects, and electron correlations, which play a crucial role in the emergence of Kitaev and Γ terms alongside the previously studied Dzyaloshinskii-Moriya and ring exchange interactions.

Spin liquids are, however, not the sole focus of nonmagnetic disordered phases in quantum magnets. There are valence-bond solids in the spin-1 chain known as symmetry-protected topological phase⁹, valence-bond crystals based on singlets in Shastley-Sutherland model^{10,11}, and spin nematic phases or a quadrupolar order triggered by the condensation of two-magnon bound state for $S = 1$ models¹²⁻¹⁴ and $S = 1/2$ or $S = 1$ spin ladders^{15,16}. Notably, some of these phases break lattice symmetry while suppressing magnetic orderings, making them experimentally more accessible compared to spin liquids. Fortunately, there exist material platforms that host these phases, such as $\kappa\text{-ET}_2\text{Cu}_2(\text{CN})_3$ ¹⁷ and $\text{ZnCu}_3(\text{OH})_6\text{Cl}_2$ ^{18,19}, for spin liquids, NENP for Haldane chain²⁰, and $\text{SrCu}_2(\text{BO}_3)_2$ ²¹ for orthogonal dimer phases, providing crucial insights into the nature of these intriguing phases governed by strong quantum fluctuations and correlations.

Despite these advancements, the role of off-diagonal

symmetric Γ terms, which have recently been observed in Yb and other 4f-based magnets, remains largely unexplored^{7,8}. Initially discussed as secondary terms in Kitaev magnets, the Γ term, in conjunction with the Heisenberg interaction, destabilizes Kitaev spin liquids in two dimensions²². In the one-dimensional analog known as the Kitaev-Heisenberg- Γ chain²³, the Γ term significantly alters the ground state phase diagram, leading to $\text{SU}(2)$ symmetric points and magnetic orderings with spontaneously oriented easy axes.

This paper elucidates the role of the Γ term in geometrically frustrated zigzag Heisenberg spin-1/2 chain, whose potential platform is the 4f insulating magnet, YbCuS_2 . Previously, we have microscopically derived the quantum spin model for this material based on the Γ_6 Kramers doublet of Yb ions that forms a zigzag chain, revealing nearly isotropic $J_1 \sim J_2$ Heisenberg interactions and small but finite Γ -type exchange couplings²⁴.

Experimentally, YbCuS_2 undergoes a first-order transition to a low-temperature phase lacking clear long-range magnetic ordering, with NMR suggesting gapless nonmagnetic excitations^{25,26}. The experimental magnetic-field-temperature phase diagram does not conform to the previous theory of the simple J_1 - J_2 Heisenberg model²⁷. Our theoretical parameterization considers the J_1 - J_2 and Γ_1 - Γ_2 zigzag chain, and unveil the entire phase diagram with and without a magnetic field, incorporating ferromagnetic, antiferromagnetic, or mixed Heisenberg exchange couplings. We employ techniques such as density matrix renormalization group (DMRG), exact diagonalization, bond-operator approach, mean-field analysis on Ising competing orders. The key finding is the emergent nonmagnetic gapless excitations introduced at an infinitesimally small value of Γ inside the robust magnetic spin gap of the dimer singlet long-range

ordered phase. On top of that, the competing various magnetically and nonmagnetically ordered phases appear as the complex interplay of geometrical frustration effect of zigzag structure and the competition of Heisenberg and Γ -terms.

The paper is structured as follows: Section II presents the model Hamiltonian and the ground-state phase diagram in detail, Section III focuses on antiferromagnetic cases and the effect of the Γ term using the bond-operator approach and mean-field analysis, Section IV outlines the magnetic phase diagram, and Section V discusses materials and experimental implications.

II. MODEL AND THE GROUND STATE PHASE DIAGRAM

A. Model Hamiltonian

We consider a quantum spin-1/2 Hamiltonian on a zigzag chain given as

$$\mathcal{H} = \sum_j \sum_{\eta=1,2} J_\eta \mathbf{S}_j \cdot \mathbf{S}_{j+\eta} + \Gamma_\eta (S_j^x S_{j+\eta}^y + S_j^y S_{j+\eta}^x), \quad (1)$$

where J_η and Γ_η are the Heisenberg and anisotropic exchange interactions between nearest ($\eta = 1$) and next nearest ($\eta = 2$) spins. We consider both the antiferromagnetic (AFM) and ferromagnetic (FM) couplings of J_η and set

$$\begin{aligned} J_1 &= \cos \phi \cos \theta, & J_2 &= \sin \phi \cos \theta, \\ \Gamma_1 &= \cos \phi \sin \theta, & \Gamma_2 &= \sin \phi \sin \theta, \end{aligned} \quad (2)$$

where dividing the parameter range into four, $\phi = [0 : \pi/2], [\pi/2 : \pi], [\pi : 3\pi/2], [3\pi/2 : 2\pi]$ correspond to AFM-AFM, FM-AFM, FM-FM, AFM-FM interactions of J_1 - J_2 , respectively. The sign of Γ_η can be converted by the local unitary transformation and does not influence the physical state. The spin quantization axis z is taken parallel to the chain (see Fig. 1).

The model at $\Gamma_\eta = 0$ corresponds to the zigzag Heisenberg spin chain, the phase diagram of which has been extensively studied previously. In the AFM-AFM case where J_1 and J_2 are both positive, there exists a transition from a Tomonaga-Luttinger liquid (TLL) phase to a dimer singlet phase characterized by a finite spin gap^{28–30}. This transition occurs at a critical point $(J_2/J_1)_c \approx 0.2411$ ($\phi \approx 0.075\pi$)^{31,32}. Within the dimer singlet phase, a Lifshitz point $(J_2/J_1)_L \approx 0.5206$ ($\phi \approx 0.153\pi$) delineates two distinct regions: one with commensurate $q = \pi$ short-range magnetic correlations and another with incommensurate $q < \pi$ correlations at lower and higher J_2/J_1 values, respectively^{33,34}. There is also an ongoing debate regarding a potential transition from the dimer phase to a gapless phase around $J_2/J_1 \approx 2.2$ ($\phi \approx 0.36\pi$), identified through level crossing experiments³⁵, exact diagonalization and density matrix

renormalization group (DMRG) studies³⁶. This observation contradicts field theory predictions, which suggest a finite gap $\Delta \sim \exp(-(J_2/J_1)^\eta)$ with $\eta = 1$ ³⁷ or $\eta = 2/3$ ³⁸ for large J_2/J_1 values. We see shortly in our phase diagram in Fig. 1(a) that the phase boundary has a kink which extrapolates to $J_2/J_1 \approx 2.2$, indicating that the phase changes its nature at $J_2/J_1 \gtrsim 2.2$. Whereas, it is numerically difficult to conclude whether there is a finite but exponentially small spin gap or not.

In the FM-AFM case, a Haldane dimer phase exists where ferromagnetic spin pairs form $S = 1$ states for $J_2/J_1 < -1/4$ ($0.922\pi < \phi < \pi$)^{39,40}. At the critical point $J_2/J_1 = -1/4$ ($\phi = 0.922\pi$), an exactly solvable resonating valence bond (RVB) state appears⁴¹, leading to a transition to a phase with ferromagnetic (FM) long-range order. Similar to the AFM-AFM case, the existence of a gap at large $J_2/|J_1|$ remains a subject of controversy^{35,40}.

For the FM-FM and AFM-FM regions, there is no frustration and the ferromagnetic and TLL phases are realized, respectively.

The zigzag XXZ chain exhibits a richer variety of phases because of the broken SU(2) symmetry, including dimer singlet, spin fluid, ferromagnetic, antiferromagnetic phases^{42–46}, and long-range order of vector chirality at large Ising anisotropy³³. Similarly, a zigzag Heisenberg ladder in an applied magnetic field also displays comparably a Tomonaga-Luttinger liquid (TLL), a 1/3-magnetization plateau, spin-density-wave, vector chiral, and fully polarized phases^{15,27,47–49}.

Here, we investigate the impact of the anisotropic exchange interaction known as the Γ term on these previously studied phases.

B. Ground-state phase diagram

1. Overview of the phase diagram

Figure 1 shows the phase diagram on the plane of $\phi = \arctan(J_2/J_1)$ and $\theta = \arctan(\Gamma_\eta/J_\eta)$. Among four different regions separated by the sign of exchange interactions (see the sign of J_1 and J_2 in the top panel), we have previously studied the AFM-AFM region ($\phi \leq 0.5$) in Ref.[50] with a particular focus on the multicritical point observed at $J_2/J_1 = 1/2, \Gamma/J = \sqrt{3}$ ($\phi \approx 0.148\pi$, $\theta = \pi/3$). This point is rigid as we find an exact solution that has degeneracy of order- N^2 as shown in Ref.[50]. It is not only a multicritical but also a Lifshitz point, because the uniform ferromagnetic (FM1) and the antiferromagnet with up-up-down-down period (AFM-UDD) meet the quantum disordered two phases, i.e. the TLL and nematic-singlet dimer phases. The low energy effective theory at around this multicritical point is shown in Appendix B, which nicely explains the Ising types of competitions among AFM-UD2 (antiferromagnet with up-down period), UDD, and FM1 phases,

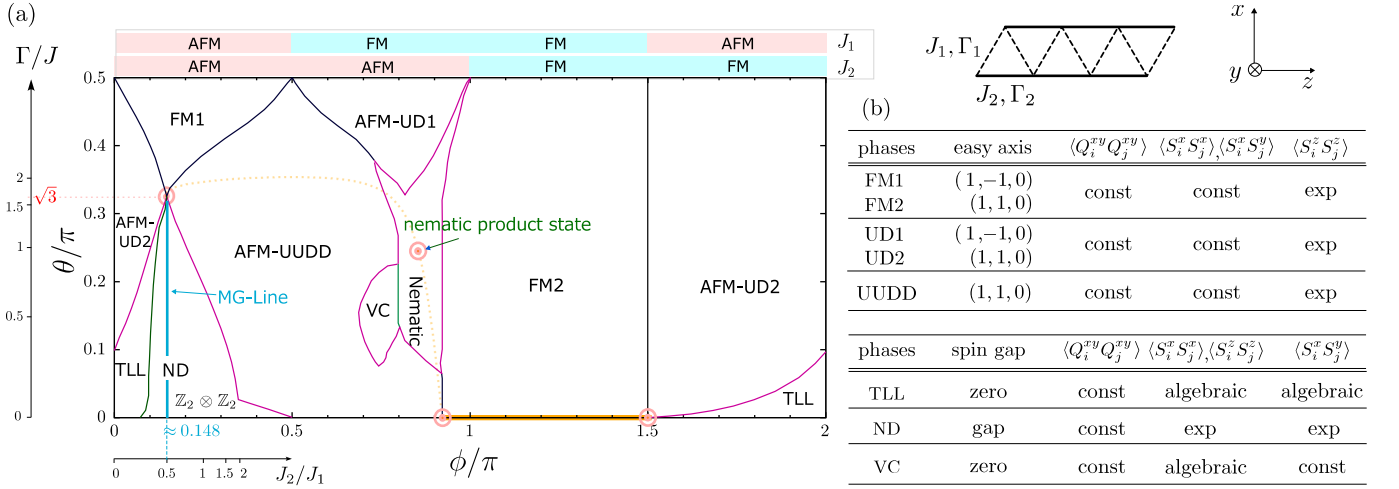


FIG. 1. (a) Ground-state phase diagram of a spin-1/2 zigzag spin chain shown in the right panel, where the z -axis parallel to the legs and the y -axis perpendicular to the triangular plane. We take $J_1 = \cos \phi \cos \theta$, $J_2 = \sin \phi \cos \theta$, $\Gamma_1 = \cos \phi \sin \theta$ and $\Gamma_2 = \sin \phi \sin \theta$. Three nonmagnetic phases are denoted as the nematic-singlet dimer (ND) phase, the Tomonaga-Luttinger liquid (TLL) phase, and vector chiral (VC) phase. Magnetically long-range ordered phases are ferromagnetic (FM), antiferromagnetic (AFM) UD, or UUDD phases. Four circles represent the exact solution points (tricritical Lifshitz point, nematic product state, RVB state, fully polarized ferromagnet), and the bold lines (Majumdar-Ghosh line and $\theta = 0$ line) are the exact solution lines. Pink and dark phase boundaries are determined by the change of magnetization and the energy crossing, respectively, and the VC and TLL-ND phases are from the scaling and vector chiral correlations, respectively. (b) Characteristics of phases in terms of magnetic order, correlation functions, and spin gap, to be detailed in Figs. 2-5.

which are summarized in Fig. 1(b). In the following subsections, we study the details of these phases.

There are three other exact solutions (see Appendix A), the nematic product state at $(\phi/\pi, \theta/\pi) = (0.852, 0.25)$ ($J_2/J_1 = -1/2, \Gamma/J = 1$), the RVB solution⁴¹, and decoupled ferromagnetic chain, which are linked by bold lines and also partially host exact solutions (for nonbroken lines). These states are obtained using the method we developed to have the exact MPS-based solutions for frustration-free models⁵¹.

Here, we briefly explain how we identify the nematic product exact ground state. At $\Gamma_\eta = J_\eta$ and $J_2/J_1 = -1/2$, the Hamiltonian has a typical frustration-free form, $\mathcal{H} = \sum_l \hat{h}_l$, given as the sum of operator \hat{h}_l acting on the l -th triangle,

$$\hat{h}_l = \sum_{i,j \in l} (-)^{|i-j|} J(\mathbf{S}_i \cdot \mathbf{S}_j + S_i^x S_j^y + S_i^y S_j^x), \quad (3)$$

where we set one AFM and two FM bonds with $J \equiv J_2$. In a triangular unit, \hat{h}_l has four-fold degenerate ground states of energy $-3J/4$ and the four excited states with energies $\pm 2(\sqrt{3}+3)J/4$. Using 0/1 representing up/down spins on $[l+1, l, l-1]$ sites on the triangle in the descending order, they are given as

$$\begin{aligned} |000\rangle + i|011\rangle &= |0\rangle \otimes (|00\rangle + i|11\rangle), \\ |000\rangle + i|110\rangle &= (|00\rangle + i|11\rangle) \otimes |0\rangle, \end{aligned} \quad (4)$$

and their time reversal states, $|111\rangle - i|100\rangle$, and $|111\rangle - i|001\rangle$. The energy of the Hamiltonian consisting of N triangles is $-3JN/4$ at the lowest, and the product state

$|\Psi\rangle = \prod_{i=1}^{N/2} |p_1\rangle_{2i-1, 2i}$, with $|p_1\rangle = (|00\rangle + i|11\rangle)/\sqrt{2}$, satisfies such energy condition, because for all choices of triangles, we find either of Eq.(4) to be the constituent. Its time reversal or translational counterparts are the other degenerate ground state. The translational symmetry is broken similarly to the Majumdar-Ghosh (MG) singlet product state at $J_2/J_1 = 0.5$. The other exact solutions in the phase diagram can be obtained in the same frustration-free form, although the other non-product state solutions are not explicitly written in the analytical form but rely on the MPS language⁵¹.

The phase diagram was determined using the DMRG method^{52,53} and the exact diagonalization (ED) method. For DMRG we calculate the system typically of size $N = 100$ and keep up to $\chi = 200$ states with up to 160 sweeps. Because the model with quantum anisotropy often exhibits orders or correlations with incommensurate or unexpected periods, we adopt the sine-square deformation (SSD)⁵⁴ that suppresses the numerical biases often induced in finite-size clusters; for any given Hamiltonian $\mathcal{H} = \sum_j \hat{h}(r_j)$ based on the local operator $\hat{h}(r_j)$ at spatial coordinate $r_j = 1, \dots, N$, the method deforms its local energy scale by the envelope function as $\mathcal{H}_{\text{ssd}} = \sum_j \hat{h}(r_j) f(r_j)$, using the $f(r_j) = \sin^2(\pi r_j/(N+1))$. This sine-square function $f(r_j)$ takes a maximum at the center of the system and goes to zero at both edges. It is proved both numerically and analytically that the SSD Hamiltonian offers a quantum ground state equivalent to that of the periodic boundary condition (PBC)⁵⁵⁻⁵⁷. Additionally, it has two advantages: the damping of the finite size effect and the ability to capture incommensurate or-

ders very accurately by avoiding the bias to wavevectors commensurate with the system size^{58,59}. The boundary effects are safely excluded and the correlation functions as well as local quantities are safely evaluated, much more reliably than the open boundary ones⁶⁰. The DMRG using SSD also can evaluate the continuous magnetization curve very accurately, which is particularly useful here because the model does not conserve the total magnetization and the standard evaluation of the spin gap as the difference in the energy of total $S = 0$ and $S = 1$ states is not available.

2. Phase boundaries

We first introduce the order parameters of the three magnetic phases and the two nonmagnetic phases in the diagram:

$$\begin{aligned}
 \text{FM} & : S_i^\alpha + S_{i+1}^\alpha + S_{i+2}^\alpha + S_{i+3}^\alpha, \\
 \text{AFM-UD} & : S_i^\alpha - S_{i+1}^\alpha + S_{i+2}^\alpha - S_{i+3}^\alpha, \\
 \text{AFM-UUDD} & : S_i^\alpha \pm S_{i+1}^\alpha - S_{i+2}^\alpha \mp S_{i+3}^\alpha, \\
 \text{VC} & : \kappa_i^{(n)} = S_i^x S_{i+n}^y - S_i^y S_{i+n}^x, \\
 \text{N} & : Q_i^{xy} = S_i^x S_{i+1}^y + S_i^y S_{i+1}^x.
 \end{aligned} \quad (5)$$

For the VC phase, we choose $\kappa_i^{(1)}$ which is the most susceptible to the present Hamiltonian. Regarding the nematic (N) phase, There are five independent nematic (quadrupolar) operators defined on a spin-1/2 pairs forming spin-1 given as⁶¹

$$Q_i^{\alpha\beta} = S_i^\alpha S_{i+1}^\beta + S_i^\beta S_{i+1}^\alpha - \frac{2}{3} (\mathbf{S}_i \cdot \mathbf{S}_{i+1}) \delta_{\alpha\beta}. \quad (6)$$

In Eq.(1), the parameter Γ is coupled to the xy component $Q_i^{xy} = S_i^x S_{i+1}^y + S_i^y S_{i+1}^x$, and it works as a “field” (or a chemical potential) to condense the nematic particle represented by Q_i^{xy} , and accordingly, the other four parameters are irrelevant.

The phase boundaries are determined numerically. The first-order transition takes place between magnetic orders of different periods and the second-order transitions are mostly the nonmagnetic-magnetic ones. We show in Fig. 2(a) the energy of the SSD Hamiltonian of the DMRG calculation for $N = 100$ as a function of ϕ . The observed kinks or the changes in the functional form provide the magnetic phase boundaries very accurately, as has been demonstrated in previous literatures^{62,63}. Namely, even if the envelope function $f(r_j)$ is placed, which will alter the value of the total energy of the system itself, because the energy is an extensive quantity, the comparison of energies between different phases works out quantitatively as accurate as we do in PBC. We can see shortly that they coincide with the ones we derive using the magnetic order parameters. The boundary between the nematic-singlet and the TLL phases is difficult to detect in standard methods. In Fig. 2(b) we show

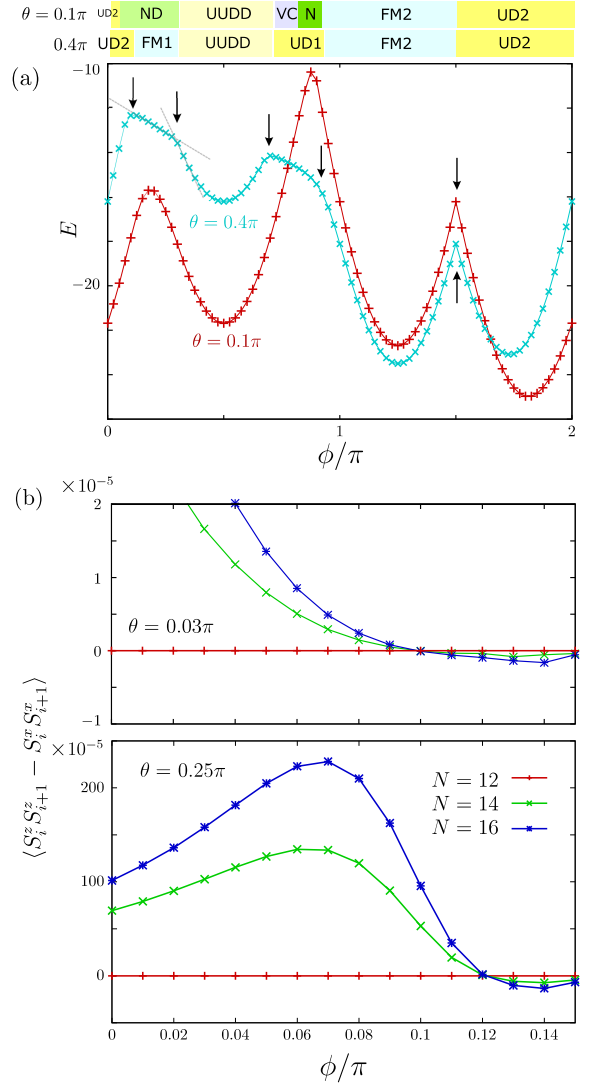


FIG. 2. (a) Energy obtained by DMRG calculation and (b) $\langle S_i^z S_{i+1}^z - S_i^x S_{i+1}^x \rangle$ obtained by the exact diagonalization with PBC as functions of ϕ . The kinks in (a) and crossings in (b) are used to determine the magnetic and nonmagnetic phase boundaries, respectively. Broken lines in panel (a) are shown as a guide to determine one of the phase boundaries.

the $\langle S_i^z S_{i+1}^z - S_i^x S_{i+1}^x \rangle$ obtained by the Lanczos exact diagonalization method, which measures the anisotropy of nearest neighbor spin coupling. We find that the results for different N 's cross at the single point, which offers accurate scale-free boundary points separating TLL-ND phases.

The magnetic phase boundaries are clearly detected by the magnetization of several lattice periods and magnetization axes. Because we use the SSD, the values of magnetization measured at the center of the system is not influenced by the boundary effect and is free of finite-size effects. Here, we measure the magnetization along the x' and y' axes which are obtained by rotating the x and y axes by $\pi/4$ about the z -axis. In-

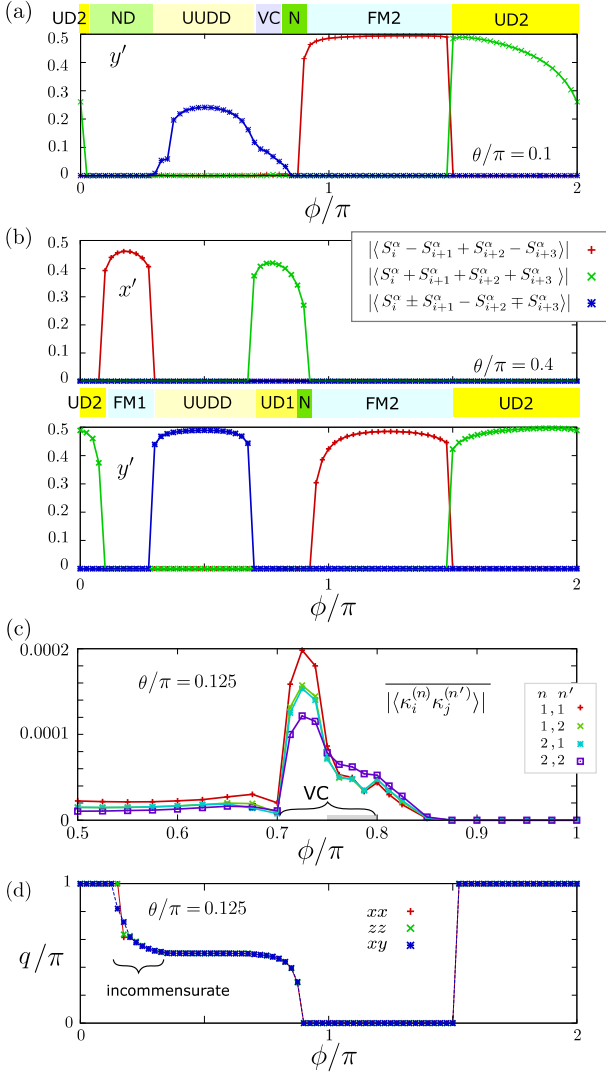


FIG. 3. Uniform and staggered magnetizations in a period of two or four sites, $S_i^\alpha + S_{i+1}^\alpha + S_{i+2}^\alpha + S_{i+3}^\alpha$, $S_i^\alpha - S_{i+1}^\alpha + S_{i+2}^\alpha - S_{i+3}^\alpha$, and $S_i^\alpha \pm S_{i+1}^\alpha - S_{i+2}^\alpha \mp S_{i+3}^\alpha$, for (a) $\theta/\pi = 0.1$ ($\Gamma/J \approx 0.32$) in $\alpha = y'$ -direction and (b) $\theta/\pi = 0.4$ ($\Gamma/J \approx 3.1$) in x' and y' -directions as functions of ϕ . (c) Vector chiral correlation function $|\langle \kappa_i^{(n)} \kappa_j^{(n')} \rangle|$ averaged over $|i-j| = 58-61$ as function ϕ . The gray region has the relatively weak signal of chiral correlation. (d) Peak position q of the structure factor $\mathcal{S}^{\alpha\alpha'}(q)$ for $\alpha\alpha' = xx, zz, xy$ as a function of ϕ . We set $\theta/\pi = 0.125$ ($\Gamma/J \approx 0.41$) for (c,d).

deed, our Hamiltonian Eq.(1) remains unchanged under the π -rotation about both the $\mathbf{x}' = (-1, 1, 0)$ and $\mathbf{y}' = (1, 1, 0)$ axes, where the spins are transformed as $(S^x, S^y, S^z) \rightarrow (-S^y, -S^x, -S^z)$ and $(S^y, S^x, -S^z)$, respectively. It is thus natural to consider the two as magnetic easy axes. We can thus introduce the order parameters of the magnetic phases as in Eq.(5). In Fig. 3, we show these uniform and staggered magnetization along $\alpha = x', y'$ for two parameters across the phase diagram. In the case of $\theta = 0.1\pi$ ($\Gamma/J \approx 0.32$), x' -component

of these magnetizations are exactly zero throughout ϕ and are not shown. Otherwise, the magnetic phases have one of the magnetizations being finite, and are exclusive to each other, capturing the phase boundaries very well. The types of magnetizations are summarized in Fig. 1(b).

In Fig. 3(d) we show the peak position of the structure factor of the two-point spin-spin correlation functions

$$\mathcal{S}^{\alpha\alpha'}(q) = \frac{1}{N-1} \sum_{|j-j'|=1}^{N-1} e^{iq(j-j')} \langle S_j^\alpha S_{j'}^{\alpha'} \rangle, \quad (7)$$

where in the calculation we performed the SSD Fourier transformation using the envelope function⁶⁴. Previous studies for the $\Gamma = 0$ zigzag model reported the transition from a $q = \pi$ to $q < \pi$ state of the diagonal $\alpha = \alpha'$ structure factor inside the singlet dimer phase^{33,34}. We indeed find such a transition for $\theta > 0$ ($\Gamma \neq 0$) in the present model. In particular, in the ND phase at $0.15 \lesssim \phi/\pi \lesssim 0.4$ ($0.5 \lesssim J_2/J_1 \lesssim 3$), the incommensurate $q \gtrsim \pi/2$ is observed which transforms to the UDD phase of period $q = \pi/2$ at larger ϕ . The difference induced by the $\Gamma \neq 0$ is that the off-diagonal xy component appears comparable to the diagonal ones.

Let us briefly discuss the types of symmetry breakings. As mentioned above, the spins have x' and y' as magnetic easy axis, namely the $\mathbb{Z}_2 \otimes \mathbb{Z}_2$ symmetry is present in the Hamiltonian. In the ND and TLL phases, the spins are not ordered, namely this $\mathbb{Z}_2 \otimes \mathbb{Z}_2$ is not broken. The ND phase breaks the translational symmetry but TLL does not. When the magnetic orderings take place, they break one of the $\mathbb{Z}_2 \otimes \mathbb{Z}_2$ (while part of \mathbb{Z}_2 combined with lattice translation remains), and the spins are polarized in one of the two easy axes. The translational symmetry is broken for the AFM phases, while kept for FM phase. The competition among different ways of symmetry breaking generates a highly competing multicritical point.

Going back to Fig. 1(a), we see that the phase diagram has approximate reflection symmetry about the $\phi = 0.5\pi$ line. By this reflection, the FM1 and AFM-UD1 phases are related and so as AFM-UD2 and FM2. The $\Gamma/J = \sqrt{3}$ tricritical point is related to another cusp point, and the TLL-singlet dimer transition point $J_2/J_1 = 0.2411, \Gamma_\eta = 0$ ($\phi = 0.075\pi, \theta = 0$) has as the counterpart the FM-Haldane dimer transition point $J_2/J_1 = -1/4$, at $\Gamma_\eta = 0$ ($\phi = 0.922\pi, \theta = 0$). The nearly-reflection symmetry of the phase diagram is described in the Hamiltonian as the conversion of all the spins on one of the two legs upside down. Since the spin inversion is a non-unitary transformation for $S = 1/2$ it is not rigorous. Indeed, the reflection symmetry is not perfect, particularly when $\theta \lesssim 0.25\pi$ ($\Gamma/J \lesssim 1$). However, considering the Ising character of the magnetic phases at large θ or Γ/J , that join the low energy effective Hamiltonian near the multicritical point (see Appendix B, it is natural to find that the phase boundaries of large θ are explained very well in this context.)

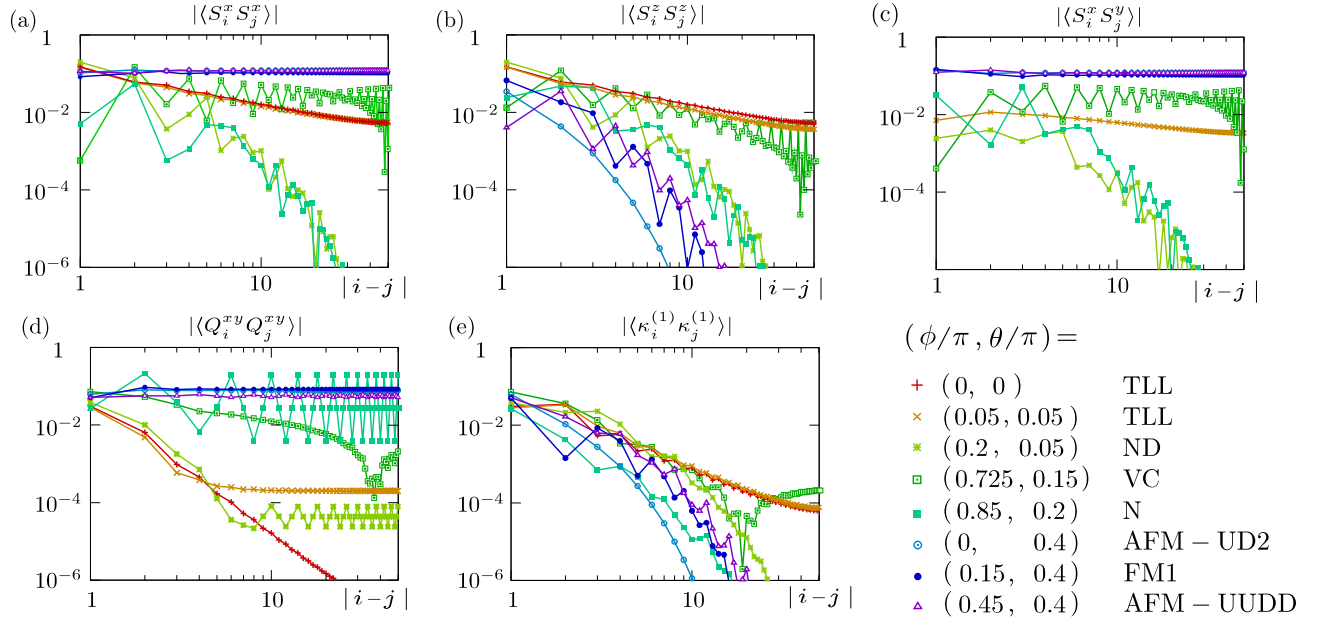


FIG. 4. Two-point correlation functions $\langle O_i O_j \rangle$ of (a)-(c) spins $O_i = S_i^{\alpha_i}$ of $(\alpha_i \alpha_j) = xx, zz$, and xy , (d) nematic operators $Q_i^{xy} = S_i^x S_{i+1}^y + S_i^y S_{i+1}^x$, and vector chiral operators (e) $\kappa_i = S_i^x S_{i+1}^y - S_i^y S_{i+1}^x$, obtained by DMRG with $N = 100$. Symbols ND, VC, N, TLL indicate the nematic dimer, vector chiral, nematic, and Tomonaga-Luttinger liquid phases, respectively. Several parameters (ϕ, θ) are chosen from nonmagnetic and magnetic phase as well as the antiferromagnetic Heisenberg chain $\phi = \theta = 0$.

3. Correlation functions

We obtain the two-point correlation functions $\langle O_i O_j \rangle$, using the single-site or two-site operator O_i . For O_i , we take spin operators, S_i^α with $\alpha = x, y, z$, vector chiral operator $\kappa_i^{(n)}$, and nematic operator Q_i^{xy} . Figure 4 shows these correlation functions as functions of distance, $|i-j|$, obtained using SSD-DMRG. Let us summarize the features of each phase.

TLL phase. Basically, the correlation functions all decay algebraically up to $|i-j| \leq 50$, where we reach half of the system size. However, at $\theta \neq 0$, $\langle Q_i^{xy} Q_j^{xy} \rangle$ shows a robust constant value at large distances, unlike the standard TLL phase. This is because if the system remains paramagnetic without any other orderings, the Γ term works as a conjugate field to induce a finite value of $\langle Q_i^{xy} \rangle$, which is obvious from Eq.(1). In that context, the emergent Q_i^{xy} is trivial as it does not break any symmetry of the Hamiltonian.

Nematic-singlet dimer (ND) phase. Along the exactly solvable MG line $J_2/J_1 = \Gamma_2/\Gamma_1 = 1/2$ at $\theta < \arctan(\sqrt{3})$, we find the dimer-product singlet states as an exact ground state, which strictly excludes other components and gives $\langle Q_i^{xy} Q_j^{xy} \rangle \rightarrow 0$. While, even when we are away from the MG line, the ND phase sustains where the magnetic correlation functions all decay exponentially, indicating the existence of a spin gap. Such gap opening is due to the breaking of translational symmetry in the same manner as the MG solution. The nematic correlation $\langle Q_i^{xy} Q_j^{xy} \rangle$ starts to converge to a small but

finite constant value at long enough distances, indicating the formation of a long-range order with $\Gamma_\eta \neq 0$, as shown in Fig. 4, whose implication will be discussed shortly.

Vector chiral (VC) phase. In the FM-AFM Heisenberg interaction range of the phase diagram at $\phi/\pi \sim 0.7-0.8$ ($J_2/J_1 = -1.3 \sim -0.72$), we find a VC phase where the magnetic order is absent and $\langle \kappa_i^{(1)} \kappa_j^{(1)} \rangle$ sustains at long distances. Its amplitude shows a large oscillation in the period of chirality over about 30 spins as can be seen from the behavior of $\langle S_i^x S_j^x \rangle$ and $\langle S_i^x S_j^y \rangle$, while the pure magnetic components decay as a power law.

Magnetically ordered phases. The FM phases, AFM-UD, and UDD phases all have their magnetic easy axis pointing in the x' or y' directions perpendicular to the leg. Indeed, the correlation functions show a clear exponential decay about $\langle S_i^z S_j^z \rangle$, while those of the in-plane elements robustly take the constant value of order-1 throughout $|i-j|$. The nematic correlation is also robust because these magnetic orderings are the condensation of the off-diagonal $S = 1$ elements.

4. Spin gap

Our model does not conserve total- S^z , in which case the spin gap cannot be evaluated by the standard treatment of measuring the lowest-energy difference between different total- S^z sectors. Instead, we apply a grand canonical approach using SSD^{58,59} that allows the access

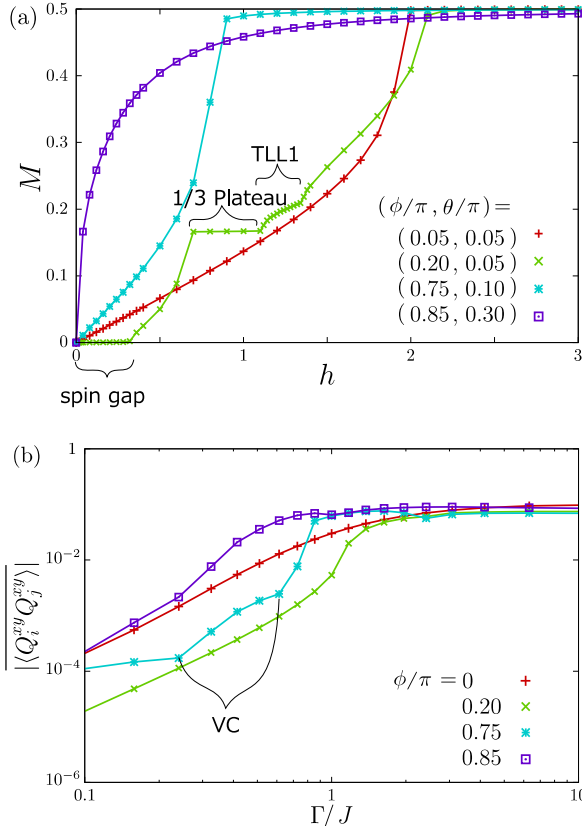


FIG. 5. (a) Magnetization curves for field h applied along the z -direction. We choose $(\phi, \theta)/\pi = (0.05, 0.05)$ ($(J_2/J_1, \Gamma/J) \approx (0.16, 0.16)$) for TLL, $(0.2, 0.05)$ ($(0.72, 0.16)$) for ND, $(0.75, 0.1)$ ($(-1.0, 0.32)$) for VC, and $(0.85, 0.3)$ ($(-0.51, 1.4)$) for N phases. Among them, only the ND phase has a spin gap $\Delta \approx 0.3$. (b) Nematic parameter $\langle Q_i^{xy} Q_j^{xy} \rangle$ averaged over $|i - j| = 58 - 61$ as a function of Γ/J for the choices of ϕ/π corresponding to those of panel (a). All of them behave in power of Γ/J .

to the bulk magnetization curve for $N \gtrsim 20$ calculations (while we adopt $N = 100$). By adding a Zeeman field $-h \sum_j S_j^z$ to Eq.(1), and by deforming them with the sine-square function, the magnetization M is obtained by extracting the intrinsic values near the center using the $q = 0$ element of the SSD Fourier transformation⁶⁴. Figure 5(a) shows four different magnetization curves obtained for the nonmagnetic ground states, TLL, ND, VC, and N. Only the ND phase shows a substantially large spin gap, $\Delta \sim 0.3$. The spin gap of $J_1 - J_2$ chain ($\Gamma = 0$) was previously calculated by DMRG³⁷ and was evaluated as $\Delta = 0.11 \sim 0.37$ for $0.14\pi < \phi < 0.25\pi$ ($0.47 < J_2/J_1 < 1.0$). For TLL and VC, the standard magnons condense and form a standard magnetization curve. Whereas, the magnetization curve of the N-phase exhibits a steep power-law increase starting from zero field, which reminds us of the magnetization curve of the ferrimagnetic-like state⁶⁵. Such a high sensitivity of magnetization shall appear because the $S = 1$ and $S^z = 1$ gapless excitation from the N phase may exist.

To confirm the presence of a finite spin gap, we examined the field-dependent magnetization in the direction of $-h \sum_j S_j^\alpha$, where $\alpha = x, y$, and x', y' ($\pi/4$ -rotation of x, y about the z -axis) as shown in Appendix C; in the ND phase, the spin gap is finite and does not depend much on the direction of a field.

5. Nematic order parameter

We have shown in Fig. 4 that the nematic correlation, $\langle Q_i^{xy} Q_j^{xy} \rangle$, starts to converge to a robust constant value once we introduce finite $\Gamma/J \neq 0$. To examine how they behave at around $\Gamma/J \sim 0$, we plot in Fig. 5(b) the averages of $\langle Q_i^{xy} Q_j^{xy} \rangle$ over $|i - j| = 58 - 61$ to exclude the strong oscillation effect⁵⁸. Numerically, there is no “gap” in the onset value of $(\langle Q_i^{xy} Q_j^{xy} \rangle)^{1/2}$, i.e. it increases immediately from $\Gamma = 0$ in power of Γ for all displayed parameters of ϕ . As mentioned, Γ in Eq.(1) works as chemical potential of nonmagnetic quasi-particle represented by the operator Q_i^{xy} .

The AFM-UDD has the staggered magnetic moment pointing in the y' direction which is nothing but the “magnetization” represented by Q^{xy} . Namely, the doped quasi-particles condense and form a regular four-fold periodic structure breaking the translational symmetry. In the ND phase, the two-fold periodic breaking of translational symmetry occurs but there is no magnetic order because of the interplay of singlet and nematic particles. The spin gap is open, which is distinct from the AFM-UDD and TLL phases.

For these reasons, we understand that “field” effect, Γ , generates a finite nematic correlation but it appears in different ways depending on the degree of frustration dictated by ϕ . As we see shortly in §.II C, the ND phase hosts gapless excitation mode due to Γ that gives the finite but small distribution of $\langle Q_i^{xy} \rangle$ in real space on top of the singlets, and at large Γ the nematic particles finally condense into the magnetically ordered phases, AFM-UD2, AFM-UDD. The TLL phase, although hosting finite nematic correlation, shall be trivial.

C. Dynamical structure factor

As we found in Fig. 5(b), the long-distant value of $\langle Q_i^{xy} Q_j^{xy} \rangle$ increases in power of Γ/J , suggesting that the nematic order parameter $\langle Q^{xy} \rangle \sim \sqrt{\langle Q_i^{xy} Q_j^{xy} \rangle}$ becomes finite by the introduction of infinitesimally small Γ/J , even for the ND phase where the singlet long-range order is present. When regarding Γ as a “field” coupled to Q^{xy} , this indicates that the ground state is gapless. To confirm it, we calculate the dynamical structure factors using the standard time-evolving block decimation

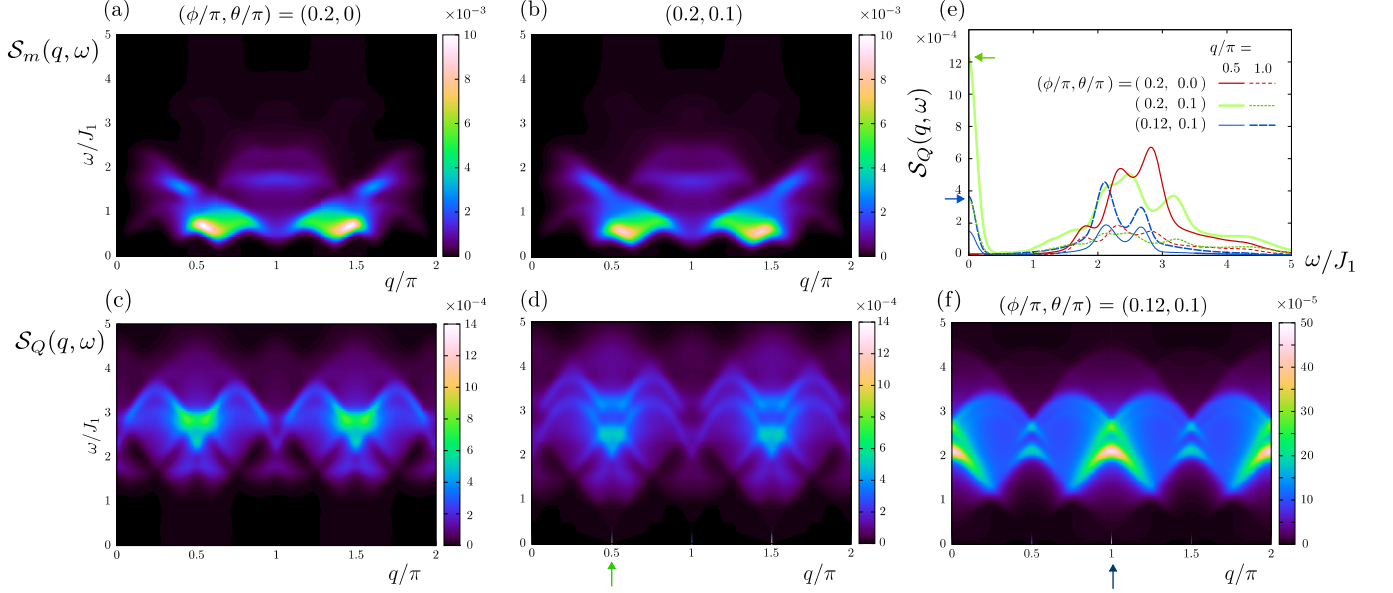


FIG. 6. (a,b) Spin and (c-f) nematic dynamical structure factors, $\mathcal{S}_m(q, \omega)$ and $\mathcal{S}_Q(q, \omega)$. For the density plots given in (a-d), we take $\phi/\pi = 0.2$ corresponding to $J_2/J_1 \approx 0.73$ with $\theta/\pi = 0$ ($\Gamma = 0$) and 0.1 ($\Gamma/J \approx 0.32$) for the pure singlet dimer and ND phases, respectively. (e) The frequency dependences of \mathcal{S}_Q are shown for fixed wave numbers, $q = \pi/2$ (solid line) and π (broken line), where we take $(\phi/\pi, \theta/\pi) = (0.2, 0), (0.2, 0.1), (0.12, 0.1)$. The green and blue arrows indicate the $q = \pi/2$ and $q = \pi$ peaks at $\omega \sim 0$, respectively. (f) The density plot of \mathcal{S}_Q at $(\phi/\pi, \theta/\pi) = (0.12, 0.1)$ ($J_2/J_1 \approx 0.40, \Gamma/J \approx 0.32$) is shown which is to be compared with panel (d).

(TEBD) technique⁶⁶ as,

$$\mathcal{S}_{m/Q}(q, \omega) = \frac{1}{N} \sum_{j=1}^N \int \frac{dt}{2\pi} e^{i(\omega t - q r_j) - \eta^2 t^2} G_{m/Q}(r_j, t), \quad (8)$$

$$\begin{aligned} G_m(r_j, t) &= \langle 0 | \mathbf{S}_j(t) \cdot \mathbf{S}_{N/2}(0) | 0 \rangle, \\ G_Q(r_j, t) &= \langle 0 | Q_j^{xy}(t) \cdot Q_{N/2}^{xy}(0) | 0 \rangle, \end{aligned} \quad (9)$$

where $|0\rangle$ the ground state of the Hamiltonian and $r_j = j - N/2$ is the one-dimensional coordinate of site j measured from the center site $N/2$. We consider two types of dynamical structure factors, $\mathcal{S}_m(q, \omega)$ and $\mathcal{S}_Q(q, \omega)$, that takes account of the magnon and nematic excitations^{67,68}, respectively. The nematic excitations are indeed detected in resonant inelastic x-ray scattering (RIXS)^{69,70}. Notice that since we take the lattice spacings between j and $j + 1$ as a unit in the Fourier transformation the reciprocal number q is defined accordingly.

We prepare an initial state $\mathbf{S}_{N/2}|0\rangle$ and $Q_{N/2}^{xy}|0\rangle$ and perform the TEBD with a timestep of $\delta t = 0.1$ up to the maximum time, $T_{\max} = 34 \sim 37$ for $N = 400$ with open boundary using the maximum bond dimension, $\chi = 400$, and the Gaussian broadening $\eta^2 = 0.004$.

Figures 6(a)-(d) show \mathcal{S}_m and \mathcal{S}_Q in the pure dimer $(\phi/\pi, \theta/\pi) = (0.2, 0)$ and nematic-singlet dimer $(0.2, 0.1)$ phases. The spin dynamical structure factors in panels (a,b) clearly show a finite gap $\Delta/J_1 \sim 0.2 - 0.3$ and the peak wave number $q \sim 0.7, 1.3$, which is consistent

with the spin gap in Figure 5(a) and the incommensurate period q_{peak} in Figure 3(d), demonstrating that the single magnon dispersion is insensitive to Γ terms. A strong peak structure is observed near $\omega = \Delta$ at $q = q_{\text{peak}}$, which is consistent with the results for the Heisenberg zigzag ladder in Ref.[71] at $J_2/J_1 = 1, \Gamma/J = 0$.

Regarding the nematic dynamical structure factor in Figs. 6(c-f), there is a distinct difference between those of zero and finite Γ ; When $\Gamma = 0$ in panel (c), the spectrum has a gap up to $\omega \sim J_1$, whereas introducing $\Gamma \neq 0$ in panel (d), there appears a new weight at $\omega \sim 0$ and $q = \pi/2$ indicated by an arrow. In Fig. 6(e), the intensity of $\mathcal{S}_Q(\omega, q)$ for fixed q is given as a function of ω , where the $\omega = 0$ peak is found to be robust. We confirmed that the peak positions are located at $q = \pi$ for $J_2/J_1 < 0.5$ and at $q = \pi/2$ for $J_2/J_1 > 0.5$, which are consistent with the ordering periods of AFM-UD2 and UDD phases, respectively, that appear in the larger Γ -part of the phase diagram.

We thus find that there is a substantial gapless low energy component carried by $\langle Q^{xy} \rangle$, which is less dispersive and conforms to the translational symmetry broken structure of single dimers. This gapless weight is the precursor for the magnetic long-range orderings that take place at large Γ/J .

III. BOND-OPERATOR MEAN-FIELD THEORY

In this section, we examine the effect of Γ -term in the AFM-AFM zigzag chain ($J_1, J_2 > 0, 0 \leq \phi \leq \pi/2$) by using bond-operator mean-field theory⁷². We see that in the Hamiltonian Eq.(1) Γ works as a “field” (or a chemical potential) to condense the nematic particle represented by Q_i^{xy} . This situation is similar to doping a magnon to the gapped singlet state⁷². The condensation of nematic particles is discussed previously, where a ring exchange interaction or frustrated interactions work as a chemical potential^{73–75}. All these cases take a gapped singlet ground state as a starting point, which is approximated by the product state of dimers (or tetramers), and the effect of the applied “field” is examined using the bond-operator approach or its analog.

We consider a model shown in Fig. 7(a) consisting of dimers (rungs) where the intra-dimer interaction is J_1, Γ_1 and the inter-dimer interactions are $\lambda J_\eta, \lambda \Gamma_\eta$, ($\eta = 1, 2$) with $0 \leq \lambda \leq 1$. The $\lambda = 1$ limit corresponds to Eq.(1). We start from $\lambda = 0$ having decoupled dimers, whose ground state is the product state of the lowest energy isolated-dimer states. By using the three excited eigenstates of the dimer represented by the three bond operators, we rewrite the Hamiltonian including the nonzero λ -terms and examine the nature of the low-energy excitations by the bond-operator mean-field theory.

A. Single dimer

The Hamiltonian of a single dimer is $\hat{h} = J_1(\mathbf{S}_1 \cdot \mathbf{S}_2 + \gamma(S_1^x S_2^y + S_1^y S_2^x))$, where we parameterize $\gamma = \Gamma_1/J_1 = \Gamma_2/J_2$. Its eigenstates are given as

$$\begin{aligned} |s\rangle &= (|\uparrow\downarrow\rangle - |\downarrow\uparrow\rangle)/\sqrt{2}, \\ |p_0\rangle &= (|\uparrow\downarrow\rangle + |\downarrow\uparrow\rangle)/\sqrt{2}, \\ |p_1\rangle &= (|\uparrow\uparrow\rangle + i|\downarrow\downarrow\rangle)/\sqrt{2}, \\ |p_{-1}\rangle &= (|\uparrow\uparrow\rangle - i|\downarrow\downarrow\rangle)/\sqrt{2}, \end{aligned} \quad (10)$$

and the corresponding eigenvalues as $\epsilon_s = 0, \epsilon_{p_0} = J_1$, and $\epsilon_{p_{\pm 1}} = J_1(1 \pm \gamma/2)$ (see Fig. 7(a)), where we dropped the constant term $-3J_1/4$ for simplicity. At $\gamma = 0$, the excited states are three-fold degenerate. The spin-singlet ground state $|s\rangle$ shows a level crossing at $\gamma = 2$ and $|p_{-1}\rangle$ replaces the ground state.

Now, we introduce the boson operators on an n -th dimer, $p_{\alpha,n}$, $\alpha = x, y, z$, together with the singlet operator s_n , which describes the four eigenstates as

$$\begin{aligned} |s\rangle_n &= s_n^\dagger |0\rangle, \\ |p_0\rangle_n &= p_{z,n}^\dagger |0\rangle, \\ |p_1\rangle_n &= \frac{e^{i3\pi/4}}{\sqrt{2}} (p_{x,n}^\dagger - p_{y,n}^\dagger) |0\rangle, \\ |p_{-1}\rangle_n &= \frac{e^{-3\pi/4}}{\sqrt{2}} (p_{x,n}^\dagger + p_{y,n}^\dagger) |0\rangle, \end{aligned} \quad (11)$$

where $|0\rangle$ is a vacuum. These operators satisfy the local constraint

$$s_n^\dagger s_n + \sum_{\alpha} p_{\alpha,n}^\dagger p_{\alpha,n} = 1. \quad (12)$$

and the commutation relations, $[s_n, s_{n'}^\dagger] = \delta_{nn'}$, $[p_{\alpha,n}, p_{\beta,n'}^\dagger] = \delta_{\alpha\beta} \delta_{nn'}$, $[s_n, p_{\alpha,n'}^\dagger] = 0$, etc.

B. Effect of inter-dimer interaction

We start from $\lambda = 0$ and $0 < \gamma < 2$, whose ground state is given as $\otimes_{n=1}^{N/2} |s\rangle_n$. We consider the system consisting of $N_d = N/2$ dimers with periodic boundary. The spin operators are described in terms of boson operators on the n -th dimer ($p_{\alpha,n}$) as

$$\begin{aligned} S_1^\alpha &= \frac{1}{2} (s_n^\dagger p_{\alpha,n} + p_{\alpha,n}^\dagger s_n - i\epsilon_{\alpha\beta\gamma} p_{\beta,n}^\dagger p_{\gamma,n}), \\ S_2^\alpha &= \frac{1}{2} (-s_n^\dagger p_{\alpha,n} - p_{\alpha,n}^\dagger s_n - i\epsilon_{\alpha\beta\gamma} p_{\beta,n}^\dagger p_{\gamma,n}), \end{aligned} \quad (13)$$

and using them, the interaction terms between the n th and $(n+1)$ th dimer, consisting of three bonds are rewritten in the form of two and four body terms, as shown in Appendix D, Eq.(D2).

Here, we consider a small λ , assuming $\gamma < 2$ ($\theta < 0.35\pi$), expecting that the ground state is dominated by singlets and the population of $p_{\alpha,n}$ -bosons are dilute. The condensed singlets are replaced by its expectation value $\langle s \rangle = \bar{s}$, and by dropping off the terms consisting of three or four p operators, we obtain the interactions between the n -th and $(n+1)$ -th dimers as

$$\begin{aligned} \hat{h}_n^{\text{MF}} &= \frac{-J_1 + 2J_2}{4} \bar{s}^2 \{ (p_{\alpha,n} + p_{\alpha,n}^\dagger)(p_{\alpha,n+1} + p_{\alpha,n+1}^\dagger) \\ &\quad + \gamma(p_{x,n} + p_{x,n}^\dagger)(p_{y,n+1} + p_{y,n+1}^\dagger) \\ &\quad + \gamma(p_{y,n} + p_{y,n}^\dagger)(p_{x,n+1} + p_{x,n+1}^\dagger) \}. \end{aligned} \quad (14)$$

C. Bond-operator mean field Hamiltonian

To fulfill the condition Eq.(12) we introduce the Lagrange multiplier μ common to all dimers, assuming the translation invariance of the system in a unit of dimer, and add the chemical potential (μ) term to the Hamiltonian. Then, we finally reach the form of the mean-field Hamiltonian consisting only of bilinear terms as

$$\begin{aligned} \mathcal{H}_{\text{bo}} &= \sum_{n=1}^{N_d} (\hat{h}_n^{\text{d}} + \hat{h}_n^{\text{MF}}) \\ \hat{h}_n^{\text{d}} &= J_1 \left(\sum_{\alpha=x,y,z} p_{\alpha,n}^\dagger p_{\alpha,n} + \gamma/2 (p_{x,n}^\dagger p_{y,n} + p_{y,n}^\dagger p_{x,n}) \right) \\ &\quad - \mu (\bar{s}^2 + \sum_{\alpha=x,y,z} p_{\alpha,n}^\dagger p_{\alpha,n} - 1). \end{aligned} \quad (15)$$

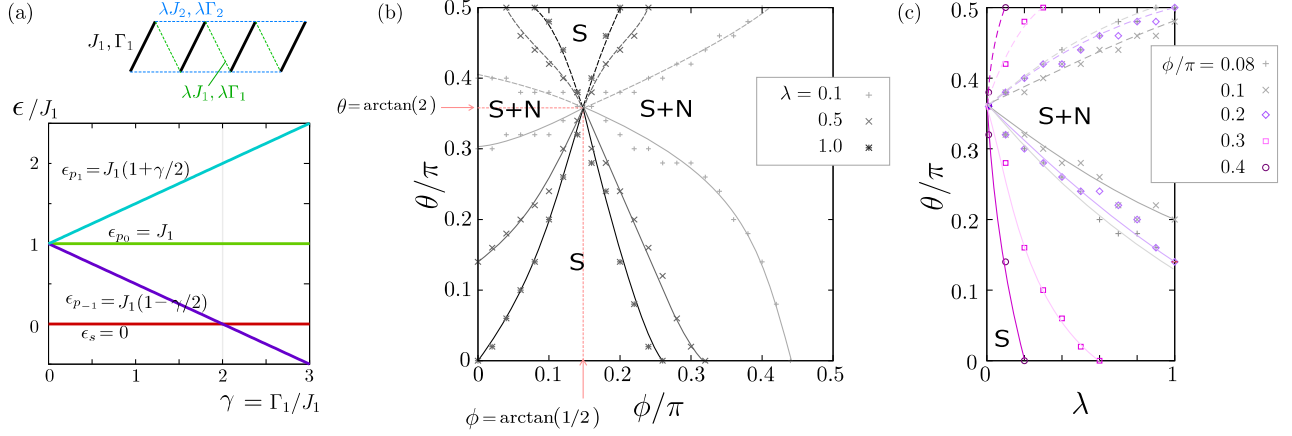


FIG. 7. (a) Zigzag lattice based on the dimer unit, where the inter-dimer interactions scaled by λ , and the eigenenergy levels of a single isolated dimer as a function of $\Gamma_1/J_1 \equiv \gamma$. Phase diagrams obtained by the bond-operator mean-field theory (b) $\theta - \phi$ plane for $\lambda = 0.1, 0.5, 1$, and (c) $\theta - \lambda$ plane for several choices of ϕ . Symbols S, S+N indicate the singlet ($\bar{s}^2 = 1$) and the nematic-singlet phase ($\bar{s}^2 < 1$).

Here, the mean-field parameters $(\mu, \bar{s}) \in \mathbb{R}$ are determined within the physically meaningful range to minimize $\langle \mathcal{H}_{\text{bo}} \rangle$.

By performing a Fourier transformation, $p_{\alpha,n}^\dagger = N_d^{-1/2} \sum_k e^{ikn} p_{\alpha,k}^\dagger$, we obtain the form,

$$\mathcal{H}_{\text{bo}} = \sum_k \{ \mathbf{u}_k^\dagger A(k) \mathbf{u}_k + \mathbf{v}_k^\dagger B(k) \mathbf{v}_k \} + N_d \left(\frac{5}{2} \mu - \frac{3}{2} J_1 - \mu \bar{s}^2 \right), \quad (16)$$

where $\mathbf{u}_k = (p_k^x, p_k^y, p_{-k}^{x\dagger}, p_{-k}^{y\dagger})^T$, $\mathbf{v}_k = (p_k^z, p_{-k}^{z\dagger})^T$, and $A(k)$, $B(k)$ are the 4×4 and 2×2 real symmetric matrices (see Appendix D).

By performing a Bogoliubov transformation, we can diagonalize \mathcal{H}_{bo} , which then yields

$$\mathcal{H}_{\text{bo}} = \sum_k \sum_{l=1}^3 \omega_l(k) \tilde{p}_{k,l}^\dagger \tilde{p}_{k,l} + E_{\text{GS}}^{\text{MF}}, \quad (17)$$

where the dispersion relations and the mean-field ground-state energy are given as

$$\begin{aligned} \omega_1(k) &= \left[(\epsilon_{p_1} - \mu) (\epsilon_{p_1} - \mu + \lambda(1 - \gamma)\varepsilon(k)) \right]^{1/2}, \\ \omega_2(k) &= \left[(\epsilon_{p_{-1}} - \mu) ((\epsilon_{p_{-1}} - \mu) + \lambda(1 + \gamma)\varepsilon(k)) \right]^{1/2}, \\ \omega_3(k) &= \left[(\epsilon_{p_0} - \mu) (\epsilon_{p_0} - \mu + \lambda\varepsilon(k)) \right]^{1/2}, \\ \varepsilon(k) &= (-J_1 + 2J_2) \bar{s}^2 \cos k. \end{aligned} \quad (18)$$

D. Phase diagram

The phase diagrams obtained by the bond-operator mean-field theory are shown in Figs. 7(b) and 7(c) for

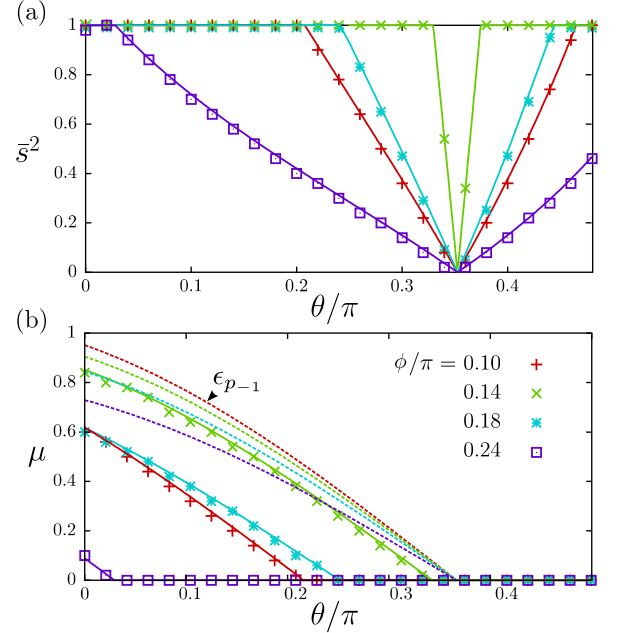


FIG. 8. The rate of singlet particle condensation \bar{s}^2 and the chemical potential μ with $\lambda = 1$.

several fixed values of $\lambda = 0.1, 0.5, 1.0$ and $\phi/\pi = 0.08$ to 0.4 ($J_2/J_1 = 0.26 - 3.1$), respectively. The corresponding set of mean-field parameters (μ, \bar{s}^2) are shown in Fig. 8 at $\lambda = 1$ as functions of θ . For these parameters, there is a range of small θ that the ground state is fully occupied by singlets, $\bar{s}^2 = 1$, which we call S-phase. The phase transition from S-phase to (S+N)-phase takes place at finite θ , where \bar{s}^2 starts to decrease from 1, and the chemical potential μ reaches the singlet (zero) energy level. When increasing λ , the S-phase shrinks because the p -particles gain the kinetic energy due to inter-dimer inter-

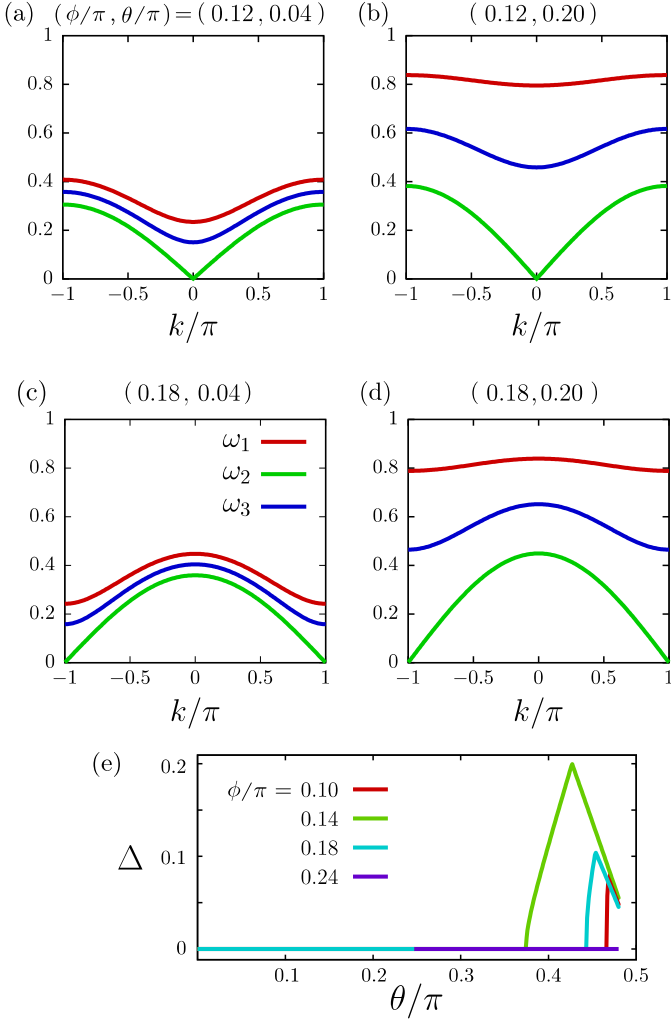


FIG. 9. (a)-(d) Dispersion relation, ω_l , $l = 1, 2, 3$ of \mathcal{H}_{bo} obtained for several choices of ϕ, θ . (e) Energy gap Δ of \mathcal{H}_{bo} normalized by $\sqrt{J_1^2 + J_2^2 + \Gamma_1^2 + \Gamma_2^2}$ as functions of θ for four choices of ϕ .

actions, but at $\phi = \text{atan}(1/2)$, i.e. $J_2/J_1 = \Gamma_2/\Gamma_1 = 0.5$, which corresponds to the Majumdar-Ghosh line, the singlet phase remains stable throughout the whole range of θ . This fact is trivial as we find that the inter-dimer interaction in Eq.(14) is $\hat{h}_n^{\text{MF}} = 0$, or equivalently, the dispersion in Eq.(18) yields $\epsilon(k) = 0$ for $J_1 = 2J_2$. Indeed, along this line, the singlet product state is the exact solution of the original Hamiltonian Eq.(1) without any approximation.

We plot in Figs. 9(a)-9(d) the energy dispersions $\omega_l(k)$ at $\lambda = 1$ for several choices of ϕ and θ , inside the S-phase. Remarkably, all of them are gapless. Indeed, the energy gap Δ of \mathcal{H}_{bo} shown in Fig. 9(e) is zero for all parameters of ϕ at small θ . This shows that the singlet phase is robust but at the same time, the p -particle are always able to join the ground state. This result is rather unusual; the standard bond operator approach is used to provide the instability toward the condensation of

these excited p -state that replaces the ground state, and the gap-closing point usually indicates the phase transition. Whereas, in the present case, the zero gap of \mathcal{H}_{bo} does not mean the instability of the singlet ground state. We emphasize that the instability takes place not at the gap closing point but when \bar{s}^2 starts to deviate from 1, and the chemical potential μ reaches the singlet energy level. For clarification, we plot in Fig. 8(b) together the bare excited energy, ϵ_{p-1} , of the isolated dimer. We see that μ is located in between ϵ_s and ϵ_{p-1} . This result is consistent with numerical results in the previous section; the coexistent nematic and singlet orders that break the translational symmetry sets in immediately when $\theta > 0$, which corresponds to the S-phase.

The ω_2 branch in Fig. 9 has a gapless point at $k = 0$ ((a,b) $J_2/J_1 < 0.5$) and $k = \pi$ ((c,d) $J_2/J_1 > 0.5$) for periods of dimer. They agree with the gapless nonzero weight of the dynamical structure factor $q = \pi$ ($J_2/J_1 < 0.5$) and $q = \pi/2$ ($J_2/J_1 > 0.5$) defined in the unit of lattice sites in Fig. 6, respectively. When θ reaches the phase boundary, the whole ω_2 branch condenses and replaces the singlet, and the magnetic long-range order in a period of the dimer (two sites) and two dimers (four sites) appear for $J_2/J_1 < 0.5$ and > 0.5 , respectively. Indeed, the phase diagram obtained by DMRG in Fig. 1(a) has AFM-UD2 and AFM-UDD phases, respectively, which are the states corresponding to S+N of different periodicity.

We may interpret that the dispersiveness of ω_2 around the gapless point shall be the artifact of the mean-field approximation to one-body because the higher order interactions and many-body effects are discarded (see Appendix D). Due to the correlation effects the weight of dispersions off the gapless point shall be weakened to form the gapless peak in the dynamical structure factor in Fig. 6.

The $p_{1,n}^\dagger$ and $p_{-1,n}^\dagger$ are the creation operator on the n -th dimer in Eq.(12) of the states that give $\langle Q_n^{xy} \rangle = 1$ and -1 , respectively. Therefore, we evaluated the number operators with respect to the eigenstate $|k, 2\rangle$ of $\omega_2(k)$, finding that

$$\langle k, 2 | p_{1,n}^\dagger p_{1,n} | k, 2 \rangle = 0, \quad \langle k, 2 | p_{-1,n}^\dagger p_{-1,n} | k, 2 \rangle = 2/N, \quad (19)$$

for all k . This indicates that each k -point carries a single $p_{-1,n}$ particle. The gapless excitation that contributes to the ground state as fluctuations thus yield the dilute order-1/ N concentration of $p_{-1,n}$, in agreement with the DMRG value of $\langle Q_i^{xy} \rangle \sim 0.01$ in Figs. 4(d) 5(b).

IV. EFFECT OF MAGNETIC FIELD

It is known that the J_1 - J_2 Heisenberg model in the AFM-AFM and FM-AFM regions exhibits a rich phase diagram in an applied magnetic field^{15,27}. Here, our Γ -terms change these phase diagrams a lot. We consider

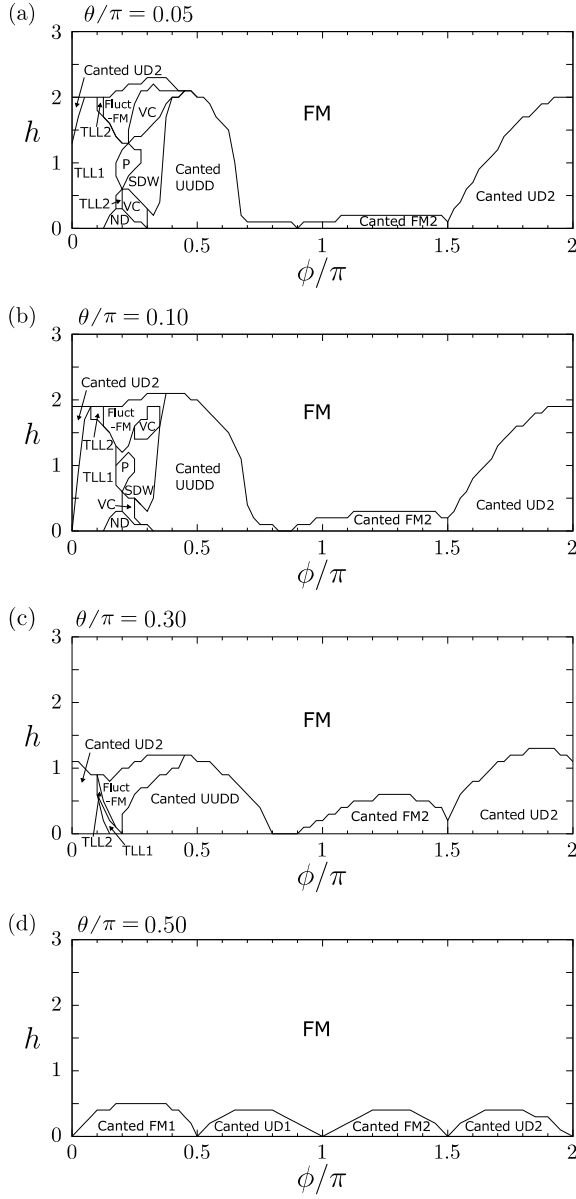


FIG. 10. Ground state phase diagram in an applied field h at (a)-(d) $\theta = 0.05\pi, 0.1\pi, 0.3\pi, 0.5\pi$ ($\Gamma/J \approx 0.16, 0.32, 1.4, \infty$). We find ferromagnetism(FM), up down(UD), fluctuating-ferro(Fluct), vector chiral(VC), Tomonaga-Luttinger liquid (TLL), spin-density wave (SDW) phases, 1/3-plateau(P), and nematic-singlet dimer(ND).

an external magnetic field along the z -axis whose Hamiltonian is given as $\mathcal{H} + \mathcal{H}_f$ using Eq.(1) with

$$\mathcal{H}_f = -h \sum_j S_j^z. \quad (20)$$

A. Magnetic phase diagram

Figure 10 shows the magnetic phase diagram at fixed values of $\theta = 0.05\pi, 0.1\pi, 0.3\pi, 0.5\pi$ ($\Gamma/J \approx$

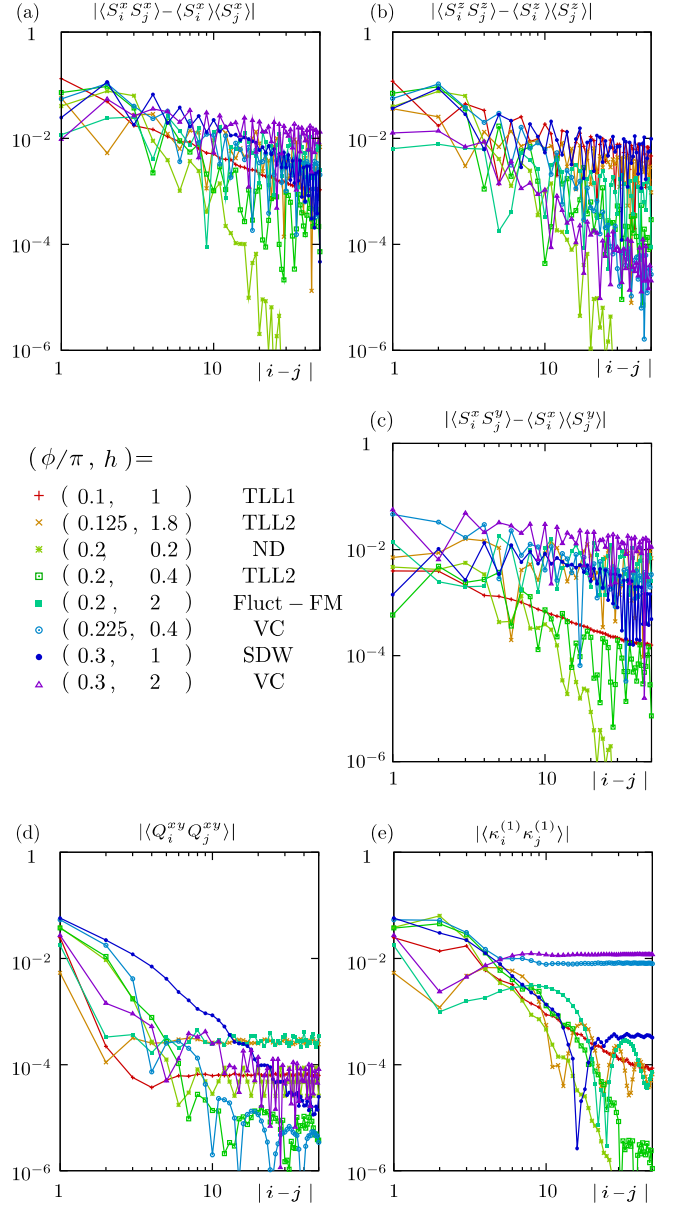


FIG. 11. Two-point correlation functions $\langle O_i O_j \rangle$ of nematic operators $O_i = S_i^x S_{i+1}^y + S_i^y S_{i+1}^x$, vector chiral operators $O_i = S_i^x S_{i+1}^y - S_i^y S_{i+1}^x$, and $\langle O_i O_j \rangle - \langle O_i \rangle \langle O_j \rangle$ of spins $O_i = S_i^{\alpha_i}$ of $(\alpha_i \alpha_j) = xx, zz$, and xy , obtained by DMRG with $N = 100$ with $\theta = 0.05\pi$ ($\Gamma/J \approx 0.16$). Symbols ND, VC, TLL, SDW, and Fluct-FM indicate the nematic dimer, vector chiral, Tomonaga-Luttinger liquid, spin-density wave and fluctuating-Ferromagnetic phases, respectively. Several parameters are chosen from nonmagnetically ordered or fluctuating FM phase.

$0.16, 0.32, 1.4, \infty$). We first focus on small Γ , namely $\theta = 0.05\pi, 0.1\pi$. Compared to the zigzag Heisenberg model, the Γ -term transforms some of the nonmagnetic phases to magnetic ordered ones. For example, the fluctuating-FM phase at around $(\phi, \theta, h) \sim (0.2, 0.05, 1.8)$ ($J_2/J_1 \approx 0.73, \Gamma/J \approx 0.16$) in Fig. 10(a) was originally a TLL2 phase²⁷ but was stabilized as an emergent small

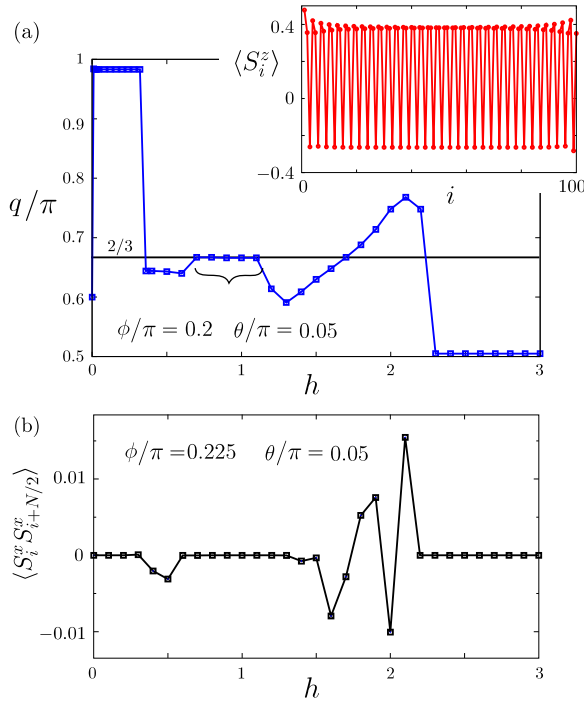


FIG. 12. (a) Local magnetization $\langle S_i^z \rangle$ (upper panel) in the 1/3-plateau phase, clearly showing the up-up-down spin configuration. The peak wave number q of $S^{zz}(q)$ is shown as a function of h , where, within $0.5\pi \leq k \leq \pi$ we find $q = 2\pi/3$. (a) The spin correlation function, $\langle S_i^x S_{i+N/2}^x \rangle \neq 0$ ($i = 25$), as a function of h that takes finite value in the fluctuating-FM phase at $1.5 \lesssim h \lesssim 2.15$.

magnetic order in the xy plane. Furthermore, in the FM-AFM region $0.5\pi < \phi < \pi$, the canted UDD phase where up-up-down-down magnetic order emerges in the xy plane, was originally a vector chiral, nematic, and other multipolar phases when $\Gamma = 0$.

At large Γ , i.e. $\theta = 0.3\pi, 0.5\pi$ in Figs. 10(c) and 10(d), the nonmagnetic phases like TLL and ND are almost wiped out. Magnetic phases, FM and UD, that appeared in the $h = 0$ phase diagram are preserved while the moments are canted off the xy -plane because of h .

B. Magnetic structures

We now summarize the features of each phase based on the two-point correlation functions shown in Fig. 11.

TLL1 and TLL2 phases. TLL1 phase is adiabatically connected to the TLL at $h = 0$. In both TLL1 and TLL2, the spin-spin correlations $\langle S_i^\alpha S_j^{\alpha'} \rangle$ show algebraic decay. The difference from those of the pure Heisenberg case is a finite $\langle Q_i^{xy} Q_j^{xy} \rangle \neq 0$ at long distances because of $\Gamma \neq 0$. The structure factor $S^{xx}(q)$ and $S^{zz}(q)$ of TLL2 show peaks at incommensurate wave numbers, whereas that of $S^{xx}(k)$ in TLL1 is commensurate. It was shown that TLL2 phase with $\Gamma = 0$ is described as two Gaussian

conformal field theory with central charge $c = 1 + 1^{27}$.

SDW phase. At large J_2/J_1 ($\phi \approx 0.3\pi$), there is a phase characterized by the incommensurate and quasi-long-ranged longitudinal correlation, $\langle S_i^z S_j^z \rangle - \langle S_i^z \rangle \langle S_j^z \rangle$, and the short-ranged transverse correlation $\langle S_i^x S_j^x \rangle$. Here, we find $\langle Q_i^{xy} Q_j^{xy} \rangle \rightarrow 0$, meaning that this type of nematic order does not exist. In the pure Heisenberg case $\Gamma = 0$, the magnetization shows a stepwise structure by $\Delta S_{\text{tot}}^z = 2$, and the exponential decay of $\langle S_i^x S_j^x \rangle$ suggests a finite energy gap to single-spin-flip excitations; they are the signature of the nematic state. However, these features are no longer observed at $\Gamma > 0$.

1/3-plateau phase. In Figs. 10(a) and 10(b), we find a 1/3-plateau phase at around $\phi/\pi \sim 0.2$ ($J_2/J_1 \sim 0.73$), which has a typical up-up-down configuration of spins. Figure 12(a) shows the wave number q at which the Fourier transform of $\langle S_j^z \rangle$ shows a peak. In our analysis, we applied the SSD Fourier transform $\langle S_q^z \rangle = \sum_{j=1}^N f(r_j) \langle S_j^z \rangle e^{-iqr_j} / \sum_{j=1}^N f(r_j)^{64}$, successfully detecting the plateau region yielding $q = 2\pi/3$.

VC and ND phases. These phases are basically the same as $h = 0$. It is also common to the case of $\Gamma = 0$ except that $\langle Q_i^{xy} Q_j^{xy} \rangle \neq 0$. The VC phase at $\Gamma = 0$ is a one-component TLL²⁷. The ND phase sustains up to finite h whose value corresponds to the spin gap at $h = 0$.

Fluctuating FM phase. The fluctuating FM phase has a ferromagnetic order with its moments pointing in the z direction and the small fluctuation in the xy plane. Its origin is essentially a Γ term because it vanishes at $\Gamma = 0$. We determined the boundary of this phase by $\langle S_i^x S_{i+N/2}^x \rangle \neq 0$ (see Fig. 12(b)).

Canted magnetic phases. The FM1, FM2, UD1, UD2, and UDD phases at $h = 0$ developed magnetic orders in the xy -plane. In a magnetic field, these moments cant in the z -directions.

V. DISCUSSION AND SUMMARY

We have elucidated the ground state phase diagram of the zigzag Heisenberg- Γ chain across regions of ferromagnetic, antiferromagnetic, and mixed couplings. Furthermore, we have depicted the magnetic phase diagram in an applied magnetic field oriented along the chain perpendicular to the Γ -type fluctuations.

In the regime where the Γ -term dominates, the model exhibits strong magnetic anisotropy, resulting in ferromagnetic (FM) and antiferromagnetic (AFM-UD, UDD) orderings with moments aligned along $(x, y, z) = (1, \pm 1, 0)$ directions, namely, in-plane and perpendicular to the chain. The application of a magnetic field tilts these moments off the plane.

In contrast, for small Γ , we observe a nematic-singlet dimer (ND) phase characterized by long-range nematic correlations and a finite spin gap. This phase features an additional nonmagnetic gapless excitation arising from the nematic correlations, as clarified by the

bond-operator mean-field theory, consistent with numerical results from DMRG simulations. The emergence of the ND phase stems from the intricate interplay between strong geometrical frustration and the Γ -term; the formation of spin singlets breaks lattice translational symmetry and impedes dominant nematic orders, while robust nematic correlations develop due to the nonmagnetic gapless nature. Ultimately, the ground state is predominantly governed by the presence of singlets. At larger and finite Γ , condensation of nematic $S = 1$ particles leads to magnetic long-range order, with spins oriented in the xy plane.

We now explore the relevance of our findings to the ytterbium-based rare-earth magnet, YbCuS_2 . The Yb ion in this material is surrounded by S_6 octahedra⁷⁶, leading to the formation of a Kramers Γ_6 doublet effectively carrying spin-1/2 due to the interplay between octahedral crystal fields of S-ions and strong spin-orbit coupling interactions²⁵. The crystal structure of YbCuS_2 is orthorhombic with space group $Pnma$ ⁷⁷, where octahedra share edges along the a -direction and every two octahedra share edges along the c -direction, forming a one-dimensional zigzag chain of Yb ions, whose details are shown in Ref.[24]. Experimental observations of the magnetic susceptibility $\chi(T)$ reveal antiferromagnetic interactions among the spins. At low temperatures, YbCuS_2 undergoes a first-order transition at $T_O = 0.95$ K, characterized by a pronounced divergence in the specific heat²⁵. In the low-temperature phase, incommensurate magnetic structures are detected through $^{63/65}\text{Cu}$ -nuclear magnetic resonance (NMR) and nuclear quadrupole resonance (NQR) measurements on polycrystalline samples²⁶. The nuclear spin-lattice relaxation rate $1/T_1$ of $^{63/65}\text{Cu}$ -NQR exhibits a T -linear behavior at $T < 0.5$ K, suggesting the presence of gapless excitations²⁶. Additionally, the magnetic-field-temperature phase diagram obtained experimentally shows a transition of the low-temperature phase to an up-up-down (UUD) phase at around 5 T²⁵.

The 1/3-plateau with up-up-down (UUD) magnetic structure is a common feature observed in triangular-based magnets, including NaYbSe_2 ^{78,79}, CsYbSe_2 ⁸⁰, RbYbSe_2 ⁸¹, and KYbSe_2 ^{79,81}. This state is typically explained by the two-dimensional $S = 1/2$ XXZ model⁸². However, in the spin-1/2 zigzag Heisenberg chain, the parameter values required for the appearance of the robust 1/3-plateau in a finite field at $h \sim J_1$ is $J_2/J_1 \sim 0.5 - 1$ that lead to a ground state dominated by the dimer singlet state in the absence of a magnetic field. This dimer singlet is fully gapped both magnetically and nonmagnetically²⁷. Consequently, this model alone cannot explain the observed nonmagnetic gapless behavior in the material.

The motivation to understand the nonmagnetic gapless behavior in YbCuS_2 led us to derive the quantum spin model of this material using perturbation theory²⁴. Specifically, we evaluated the super-exchange interactions between Yb spins mediated by S-ions through

fourth-order processes. Our analysis revealed that the diagonal exchange interaction is nearly Heisenberg-like, with a small off-diagonal Γ -type term.

The presence of this off-diagonal anisotropic interaction can be attributed to two main factors. Firstly, the large splitting of f^{12} states selects a particular orbital momentum to join the perturbation process. Secondly, slight distortions of the octahedron result in anisotropic Yb-S orbital overlap. Both effects work together to select specific spatially anisotropic orbitals that participate in electron exchange processes.

Our analysis yielded an average ratio of $\overline{J_2}/\overline{J_1} = 0.9 \sim 1.0$ and a typical ratio of $\overline{\Gamma_\eta}/\overline{J_\eta} = 0.01 \sim 0.05$. However, the precise values may vary due to potential ambiguities in the lattice parameters of the material. The resulting Hamiltonian, expressed as Eq.(1), is a simplification of the derived Hamiltonian XYZ+(off-diagonal) to the XXX+(xy+yx) model with $\Gamma_1/J_1 = \Gamma_2/J_2$. Despite this simplification, we believe that our findings provide a sound explanation for the experimental observations in YbCuS_2 .

Based on our calculations with reference parameters $\phi_{\text{Yb}} = 0.23\pi$ - 0.25π and $\theta_{\text{Yb}} = 0.003\pi$ - 0.016π for YbCuS_2 , and by comparing the phase diagram in Fig.1(a), we conclude that YbCuS_2 indeed hosts the ND phase, which comprehensively explains the experimental features reported thus far. Firstly, our calculations at ϕ_{Yb} and θ_{Yb} reveal the structure factors of longitudinal $\langle S_i^z S_j^z \rangle$ and transverse $\langle S_i^x S_j^y \rangle$ correlations with an incommensurate wave number $q \sim 0.55\pi$ - 0.6π , which closely matches the experimentally reported wave number $k = (0.305, 0.0)$ corresponding to $q = 0.61\pi$ in the leg direction⁸³. It may worth noting that such incommensurate diagonal zz, xx correlations exists for $\Gamma = 0$ ^{33,34} but the xy ones are not and may have relevance to the rotating magnetic structure in the xy plane.

Most importantly, our nematic-dimer (ND) state exhibits a robust spin-gapped singlet coexisting with a fluctuating nematic component, giving rise to the observed nonmagnetic gapless excitation that explains the T -linear behavior of $1/T_1$ in the $^{63/65}\text{Cu}$ -NQR. Furthermore, this state transforms into a 1/3-plateau phase at a critical field $h \sim J_1/2$ in our phase diagram. In the experimental context, the average Curie-Weiss temperature is approximately 30 K, and the critical field of the plateau phase is 5 T, aligning well with our numerical predictions.

Finally, we emphasize the theoretically intriguing aspect of the ND phase in our phase diagram. In the standard nematic phase observed in spin ladders, the one-particle magnon excitation is gapped while the two-magnon excitation is gapless^{15,16}. It typically occurs due to the localization of magnons caused by frustration-induced hopping cancellation. In such cases, the two-magnon bound state tends to condense earlier than the individual magnons, particularly near the saturation field⁸⁴. In our model, the spin gap or a quasi-one-magnon gap in the non-conserved S^z indeed occurs by the localization of spin-1/2 singlet pairs due to the frustration ef-

fect, breaking the lattice symmetry. However, the corresponding one-magnon instability does not compete with the quasi-two-magnon instability, as the corresponding S^z -oriented magnetic order never occurs in our phase diagram. This fact allows the unusual coexistence of the spin gap and the nonmagnetic gapless excitation in a wide range of parameters in the phase diagram. As we have discussed in §.II B 2, the ND phase has $\mathbb{Z}_2 \otimes \mathbb{Z}_2$ but breaks the translational symmetry. The former breaks at the magnetic phase transition, and the latter further breaks or recovers, depending on which of the magnetic phases to enter. This kind of phenomena may have similarity with the layers of discussions on the several symmetry-breakings reported in the Heisenberg spin ladder with the Dzyaloshinskii-Moriya interaction⁸⁵.

ACKNOWLEDGMENTS

We thank Takahiro Onimaru, Chikako Moriyoshi, Kenji Ishida, Shunsaku Kitagawa, Fumiya Hori, and Karlo Penc for discussions. This work is supported by the "The Natural Laws of Extreme Universe" (No. JP21H05191) KAKENHI for Transformative Areas from JSPS of Japan, and JSPS KAKENHI Grant No. JP21K03440.

Appendix A: Exact solutions

The phase diagram in Fig. 1(a) has multiple exact solutions: the MG line, MPS solution at the multicritical point⁵⁰, the nematic product state, the resonating valence bond state (RVB)⁴¹, the fully-polarized ferromagnetic state, and the product of the fully-polarized ferromagnetic states of the decomposed two chains.

Majumdar-Ghosh(MG) line and multicritical point. The $J_2/J_1 = \Gamma_2/\Gamma_1 = 1/2$ is a MG line hosting singlet product state as an exact eigenstate, $|\Psi_{\text{MG}}\rangle = \prod_{j=1}^{N/2} |s_j\rangle$ with $|s_j\rangle = (|\uparrow\downarrow\rangle - |\downarrow\uparrow\rangle)/\sqrt{2}$ on $[2j-1, 2j]$ sites. The $\theta = 0$ limit is the Majumdar-Ghosh model^{28,29}, and the upper endpoint with $\Gamma_\gamma/J_\gamma = \sqrt{3}$ is the multicritical point ($\phi = 0.1476\pi$, $\theta = \pi/3$), with a ground state degeneracy of $(N+2)^2/4$ (even N), $(N+1)(N+3)/4$ (odd N) for an open boundary. The exact ground state can be obtained up to $N \sim 100$, with ~ 3000 -fold degeneracy. The details of the method are given in Ref.[51].

Nematic product state. The exact ground state is found at the isolated point $\Gamma_\gamma/J_\gamma = 1$ and $J_2/J_1 = -1/2$, ($\phi = 0.852\pi$, $\theta = 0.25\pi$), at the center of the nematic (N) phase. Its form is given as $|\Psi\rangle = \prod_{i=1}^{N/2} |p_1\rangle_{2i-1, 2i}$. Here, $|p_1\rangle = (|00\rangle + i|11\rangle)/\sqrt{2}$ is the eigenstate of the nematic order parameter $Q^{xy} = S_1^x S_2^y + S_1^y S_2^x$ with an eigenvalue 1/2.

$\Gamma = 0$ exact solutions. We briefly review the previously known exact ground state at $J_2/J_1 = -1/4$, $\Gamma = 0$ ($\phi = 0.9220\pi$, $\theta = 0$). This point is at the bound-

ary of the Haldane-dimer and ferromagnetic phases, and for PBC, the fully polarized $S_{\text{tot}} = N/2$ state coexist with the nontrivial UDRVB state with $S_{\text{tot}} = 0$ which is analytically described by the equal weight superposition of all different choices of dimer covering states as $|\psi_{\text{UDRVB}}\rangle = \sum_{i < j} \sum_{k < l} \cdots \sum_{m < n} [i, j][k, l] \cdots [m, n]$ where $[i, j] = (|01\rangle_{i,j} - |10\rangle_{i,j})/\sqrt{2}$. Along the line $0.9220\pi < \phi < 1.5\pi$ with PBC the $S_{\text{tot}} = N/2$ state continues to be the ground state. At the point $\phi = 1.5\pi$ the zigzag chain is decomposed to the two ferromagnetic Heisenberg chains and the ground state is the product of two ferromagnetic chains.

Consider a unit triangle consisting of three sites, $[l-1, l, l+1]$, and define a Hamiltonian h_l as

$$\begin{aligned} h_l = & \frac{J_1}{2} (\mathbf{S}_{l-1} \cdot \mathbf{S}_l + \mathbf{S}_l \cdot \mathbf{S}_{l+1}) + \frac{J_2}{2} \mathbf{S}_{l-1} \cdot \mathbf{S}_{l+1}, \\ & + \frac{\Gamma_1}{2} (S_{l-1}^x S_l^y + S_{l-1}^y S_l^x + S_l^x S_{l+1}^y + S_l^y S_{l+1}^x) \\ & + \frac{\Gamma_2}{2} (S_{l-1}^x S_{l+1}^y + S_{l-1}^y S_{l+1}^x). \end{aligned} \quad (\text{A1})$$

When diagonalizing h_l , we find that the lowest energy state has degeneracy of $D_g = 6$ for the exact solution points and $D_g = 4$ for the lines that connect the points. Along the solid lines the system has exact solutions and its subspace is the D_g lowest energy state. The broken lines do not have the exact solutions. The relevance with Eq.(A1) and the exact solutions are explained in detail in Ref.[51], while we can explain here that the exact solution points are related and are not isolated.

Appendix B: Mean field approach around a multicritical point

At around the multicritical point in the phase diagram, the J_1 - J_2 - Γ_1 - Γ_2 model described by Eq.(1) suffers a competition among several orders. The magnetic orders to be considered here are ferromagnet (FM), two antiferromagnets with UD2 and UDD configurations, and to accommodate all of them on equal footing, we need to consider the periodicity of magnetic moments up to four sites. The coordinate of the lattice sites are taken as $R = (4n-3)a, \dots, 4na$ with lattice constant a where $n = 1, \dots, N/4$ is the unit cell index as shown in Fig. 13(a). We rely on the philosophy that the fluctuations around each order take place in a way that the magnetic moments belonging to the same magnetic sublattice are predominantly ferromagnetic.

We implement a scheme following Nelson and Fisher⁸⁶ that takes a continuum limit, $S_j \rightarrow \mathbf{S}(R)$, by retaining distinguishable four sublattices. The Hamiltonian in Eq.(1) in the main text is rewritten as

$$\begin{aligned} \mathcal{H} = & \frac{1}{2} \sum_{R, R'} \{ J(R-R') \mathbf{S}(R) \cdot \mathbf{S}(R') \\ & + \Gamma(R-R') (S^x(R) S^y(R') + S^y(R) S^x(R')) \}. \end{aligned} \quad (\text{B1})$$

Then, we transform the spins as

$$S^x = S^{x'} \cos(\pi/4) + S^{y'} \sin(\pi/4), \quad (\text{B2})$$

$$S^y = -S^{x'} \sin(\pi/4) + S^{y'} \cos(\pi/4), \quad (\text{B3})$$

which is the rotation of xy -axes by $\pi/4$ about the z -axis where we adopt $x'y'z$ -axes for spin coordinates in the following to distinguish from the original xyz -axes. Then, we find

$$\begin{aligned} \mathcal{H}^{\pi/4} = & \frac{1}{2} \sum_{R,R'} \{J(R-R') \mathbf{S}(R) \cdot \mathbf{S}(R') \\ & - \Gamma(R-R') (S^{x'}(R) S^{x'}(R') - S^{y'}(R) S^{y'}(R'))\}. \end{aligned} \quad (\text{B4})$$

We now introduce the following unitary transformation about the spin operators inside the unit cell as

$$\begin{pmatrix} \mathbf{S}_{1,n} \\ \mathbf{S}_{2,n} \\ \mathbf{S}_{3,n} \\ \mathbf{S}_{4,n} \end{pmatrix} = \frac{1}{4} \begin{pmatrix} 1 & 1 & 1 & 1 \\ 1 & -1 & 1 & -1 \\ 1 & 1 & -1 & -1 \\ 1 & -1 & -1 & 1 \end{pmatrix} \begin{pmatrix} \mathbf{S}((4n-3)a) \\ \mathbf{S}((4n-2)a) \\ \mathbf{S}((4n-1)a) \\ \mathbf{S}(4na) \end{pmatrix}. \quad (\text{B5})$$

The Fourier transformation for these new spin variables are

$$\mathbf{S}_\nu(q) = \sum_{n=1}^{N/4} e^{iq4na} \mathbf{S}_{\nu,n}, \quad (\text{B6})$$

where q runs over a folded Brillouin zone :

$$|q| \leq \frac{\pi}{4a}. \quad (\text{B7})$$

When $\langle \mathbf{S}_\nu(q) \rangle \neq 0$ we have magnetic orderings, where $\nu = 1, 2, 3$, and 4 correspond to ferromagnet ($\nu = 1$), UD antiferromagnet ($\nu = 2$), and UDD antiferromagnet ($\nu = 3, 4$).

Substituting Eqs.(B5,B6) to Eq.(B4) we find

$$\mathcal{H}^{\pi/4} = \frac{4}{N} \sum_{i,j} \sum_q \sum_\alpha \{r_{ij,\alpha=x',y',z}(q) S_{i\alpha}(q) S_{j\alpha}(-q)\}, \quad (\text{B8})$$

with couplings given as

$$\begin{aligned} r_{11,x'}(q) &= (J_1 - \Gamma_1)(3 + \cos(4qa)) \\ &\quad + (J_2 - \Gamma_2)(2 + 2\cos(4qa)), \\ r_{22,x'}(q) &= -(J_1 - \Gamma_1)(3 + \cos(4qa)) \\ &\quad + (J_2 - \Gamma_2)(2 + 2\cos(4qa)), \\ r_{33,x'}(q) &= (J_1 - \Gamma_1)(1 - \cos(4qa)) \\ &\quad - (J_2 - \Gamma_2)(2 + 2\cos(4qa)), \\ r_{44,x'}(q) &= -(J_1 - \Gamma_1)(1 - \cos(4qa)) \\ &\quad - (J_2 - \Gamma_2)(2 + 2\cos(4qa)), \\ r_{12,x'}(q) &= -r_{21,x'}(q) = (J_1 - \Gamma_1)i \sin(4qa), \\ r_{13,x'}(q) &= -r_{31,x'}(q) = (J_1 - \Gamma_1)i \sin(4qa) \\ &\quad + (J_2 - \Gamma_2)2i \sin(4qa), \\ r_{14,x'}(q) &= r_{41,x'}(q) = -(J_1 - \Gamma_1)(1 - \cos(4qa)), \\ r_{23,x'}(q) &= r_{32,x'}(q) = (J_1 - \Gamma_1)(1 - \cos(4qa)), \\ r_{24,x'}(q) &= -r_{42,x'}(q) = (J_1 - \Gamma_1)i \sin(4qa) \\ &\quad + (J_2 - \Gamma_2)2i \sin(4qa), \\ r_{34,x'}(q) &= -r_{43,x'}(q) = (J_1 - \Gamma_1)i \sin(4qa). \end{aligned} \quad (\text{B9})$$

The other couplings are related to those above; $r_{ij,y'}(q)$ are obtained from $r_{ij,x'}$ by taking $\Gamma_\eta \rightarrow -\Gamma_\eta$, and the $r_{ij,z}(q)$ are given by taking $\Gamma_\eta \rightarrow 0$.

At the multicritical point, we have $J_1 = 2J_2 \equiv J$, $\Gamma_1 = 2\Gamma_2 = 2J$. The remarkable feature of Eq.(B8) is that different spin components do not couple, which means that the competitions among different Ising orders take place. They are exclusive and the ones that contribute to the lowest energy modes are $r_{11,x'}(q)$, $r_{22,y'}(q)$, $r_{33,y'}(q)$, and $r_{44,y'}(q)$. Therefore, we can only leave these modes around the critical point and taking the $q \sim 0$ modes, we find

$$\mathcal{H}^{\pi/4} \sim \frac{1}{N} \left(r_{11,x'} S_{1x'} S_{1x'} + r_{22,y'} S_{2y'} S_{2y'} + r_{33,y'} S_{3y'} S_{3y'} \right) \quad (\text{B10})$$

where we dropped off $r_{44,y'}$ because the UDDU is equivalent to UDD of $r_{33,y'}$, related by the translation. Here, we regard the spins as classical fields in the range $-N/4 \leq S_{i\alpha} \leq N/4$, and they take the minimum or maximum at $S_{i\alpha} = 0, \pm N/4$. We thus have only three modes that contribute to the low energy excitation at the multicritical point.

The energies of the ordered state $i\alpha$ are given as $E_{i\alpha} = r_{ii,\alpha}(0)N/16$, which are explicitly written as

$$\begin{aligned} E_{1x} &= \frac{N}{4} (J_1 - \Gamma_1 + J_2 - \Gamma_2), \quad (\text{FM}) \\ E_{2y} &= \frac{N}{4} (-J_1 - \Gamma_1 + J_2 + \Gamma_2), \quad (\text{AFM-UD}) \\ E_{3y} &= \frac{N}{4} (-J_2 - \Gamma_2). \quad (\text{AFM-UDD}) \end{aligned} \quad (\text{B11})$$

The competition of these three energies yields the phase diagram shown in Fig. 13(b). Combined with the Fig 7(b), it will explain the basic feature of the numerically accurate phase diagram in Fig. 1(a).

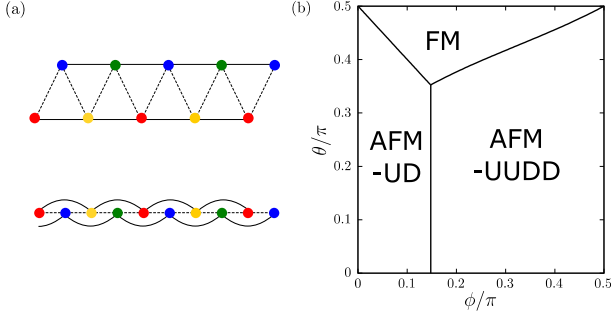


FIG. 13. (a) Schematic illustration of coarse-graining a model with four sublattices. (b) Mean-field phase diagram obtained by the competition of energies in Eq.(B11).

We note that Eq.(B11) provides the same energies as the energy expectation values of the original Hamiltonian Eq.(1) about the trial product wave functions of the corresponding FM1 phase, the AFM-UD2 phase the UDD phase, e.g. $E_{1x} = \langle \Psi_{\text{FM}} | \mathcal{H} | \Psi_{\text{FM}} \rangle$

$$|\Psi_{\text{FM}}\rangle = \prod_{j=1}^N |f\rangle_j, \quad |\Psi_{\text{UD}}\rangle = \prod_{j=1}^{N/2} |u\rangle_{2j-1} |d\rangle_{2j},$$

$$|\Psi_{\text{UDD}}\rangle = \prod_{j=1}^{N/4} |u\rangle_{4j-3} |u\rangle_{4j-2} |d\rangle_{4j-1} |d\rangle_{4j}, \quad (\text{B12})$$

where $|u\rangle_j = |\uparrow\rangle_j + e^{i\pi/4} |\downarrow\rangle_j$, $|d\rangle_j = |\uparrow\rangle_j - e^{i\pi/4} |\downarrow\rangle_j$, $|f\rangle_j = |\uparrow\rangle_j + e^{i3\pi/4} |\downarrow\rangle_j$ where the spin orientations are described in the xyz -frame and their magnetic moment points in the $(\pm 1, \pm 1, 0)$ and $(\pm 1, \mp 1, 0)$ directions, respectively.

Appendix C: Spin gap for various directions of magnetic field

Because the z -axis is a magnetic easy axis, the application of a magnetic field to the z -direction shown in Fig. 5 may naturally open a spin gap. Whereas, the field applied inside the xy plane may not necessarily be the case because the system does not magnetically order inside the xy plane in the ND phase. We thus apply a field in the four different directions, $\alpha = x, y, x'$, and y' , where the latter two are the magnetic easy axes of the FM1, UD1 (x') and FM2, UD2, UDD (y'). We add the Zeeman term in these directions, $-h \sum_i S_i^\alpha$, and measure M_α using SSD-DMRG. Figure 14 shows the magnetization curves for the four cases. We find that ND phase has a robust spin gap which does not depend much on the field direction, confirming the finite spin gap. We also show that TLL and UDD phases are gapless. In the FM1 phase, the finite magnetization in the x' -direction from $h = 0$ is observed.

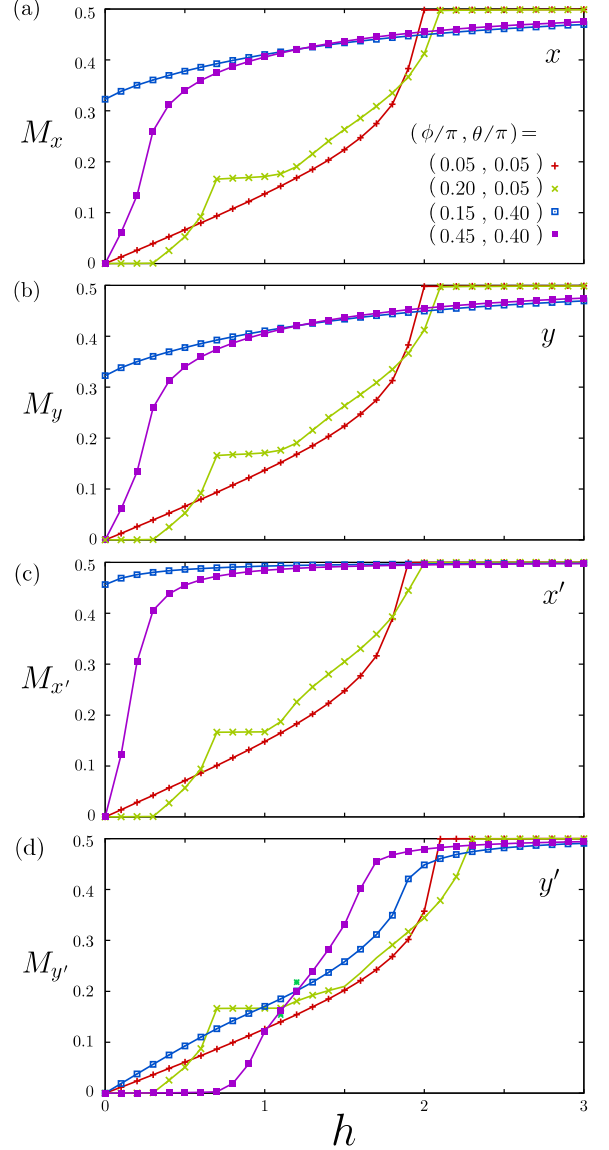


FIG. 14. Magnetization curves for field h applied along the (a) x , (b) y , (c) x' , and (d) y' -directions. We choose $(\phi, \theta)/\pi = (0.05, 0.05)$ for TLL, $(0.2, 0.05)$ for ND, $(0.15, 0.4)$ for FM1, and $(0.45, 0.4)$ for AFM-UDD phases.

Appendix D: Details of bond operator mean-field calculation

We present here the details of the bond-operator mean-field calculation in Section III.

a. Derivation of \mathcal{H}_{bo}

We first show the approximation we made in deriving the mean-field Hamiltonian \mathcal{H}_{bo} . From Eq.(13), the commutation relations, and the constraint Eq.(12), we can

rewrite the three inter-dimer spin-spin coupling terms as

$$\begin{aligned} [S_1^\alpha, S_1^\beta] &= i\epsilon_{\alpha\beta\gamma} S_1^\gamma, \quad [S_2^\alpha, S_2^\beta] = i\epsilon_{\alpha\beta\gamma} S_2^\gamma, \\ [S_1^\alpha, S_2^\beta] &= 0, \end{aligned} \quad (D1)$$

$$\begin{aligned} S_1^\alpha S_1^\alpha &= \frac{3}{4} + \frac{1}{4}(s^\dagger s^\dagger p_\alpha p_\alpha + s s p_\alpha^\dagger p_\alpha^\dagger \\ &\quad - \sum_{\substack{\beta \neq \gamma \\ x,y,z}} p_\beta^\dagger p_\beta^\dagger p_\gamma p_\gamma) \\ &\quad - \frac{1}{2} i\epsilon_{\alpha\beta\gamma} (s^\dagger p_\alpha p_\beta^\dagger p_\gamma + s p_\alpha^\dagger p_\beta^\dagger p_\gamma), \\ S_2^\alpha S_2^\alpha &= \frac{3}{4} + \frac{1}{4}(s^\dagger s^\dagger p_\alpha p_\alpha + s s p_\alpha^\dagger p_\alpha^\dagger \\ &\quad - \sum_{\substack{\beta \neq \gamma \\ x,y,z}} p_\beta^\dagger p_\beta^\dagger p_\gamma p_\gamma) \\ &\quad + \frac{1}{2} i\epsilon_{\alpha\beta\gamma} (s^\dagger p_\alpha p_\beta^\dagger p_\gamma + s p_\alpha^\dagger p_\beta^\dagger p_\gamma), \\ S_1^\alpha S_2^\alpha &= -\frac{3}{4} s^\dagger s + \frac{1}{4} p_\alpha^\dagger p_\alpha - \frac{1}{4} (s^\dagger s^\dagger p_\alpha p_\alpha \\ &\quad + s s p_\alpha^\dagger p_\alpha^\dagger \\ &\quad + \sum_{\substack{\beta \neq \gamma \\ x,y,z}} p_\beta^\dagger p_\beta^\dagger p_\gamma p_\gamma), \end{aligned} \quad (D2)$$

b. Diagonalizing Eq.(16)

We explicitly show the form of the matrices consisting Eq.(16) as

$$A(k) = \begin{pmatrix} a(k) & c(k) & b(k) & d(k) \\ c(k) & a(k) & d(k) & b(k) \\ b(k) & d(k) & a(k) & c(k) \\ d(k) & b(k) & c(k) & a(k) \end{pmatrix} \quad (D3)$$

$$B(k) = \begin{pmatrix} a(k) & b(k) \\ b(k) & a(k) \end{pmatrix}, \quad (D4)$$

$$a(k) = \frac{J_1 - \mu}{2} + \lambda \frac{-J_1 + 2J_2}{4} \bar{s}^2 \cos k\hat{z}, \quad (D5)$$

$$b(k) = \lambda \frac{-J_1 + 2J_2}{4} \bar{s}^2 \cos k\hat{z}, \quad (D6)$$

$$c(k) = -\frac{J_1}{4} \gamma + \lambda \frac{-J_1 + 2J_2}{4} \gamma \bar{s}^2 \cos k\hat{z}, \quad (D7)$$

$$d(k) = \lambda \frac{-J_1 + 2J_2}{4} \gamma \bar{s}^2 \cos k\hat{z}, \quad (D8)$$

Using a 4×4 real matrix L_k and a 2×2 real matrix M_k , we can diagonalize $A(k)$ by the Bogoliubov transformation:

$$\begin{aligned} L_k \mathbf{u}_k &= \mathbf{u}'_k, \\ \mathbf{u}'_k &= (\tilde{p}_{k,1}, \tilde{p}_{k,2}, \tilde{p}_{-k,1}^\dagger, \tilde{p}_{-k,2}^\dagger)^T, \end{aligned} \quad (D9)$$

$$\begin{aligned} M_k \mathbf{v}_k &= \mathbf{v}'_k, \\ \mathbf{v}'_k &= (\tilde{p}_{k,3}, \tilde{p}_{-k,3}^\dagger)^T. \end{aligned} \quad (D10)$$

Then, we find that

$$\begin{aligned} \sum_k \mathbf{u}_k^\dagger A(k) \mathbf{u}_k \\ = \sum_k \left(\omega_1(k) \tilde{p}_{k,1}^\dagger \tilde{p}_{k,1} + \omega_2(k) \tilde{p}_{k,2}^\dagger \tilde{p}_{k,2} + \frac{\omega_1(k) + \omega_2(k)}{2} \right), \end{aligned} \quad (D11)$$

$$\omega_1 = 2\sqrt{(a+c)^2 - (b+d)^2}, \quad (D12)$$

$$\omega_2 = 2\sqrt{(a-c)^2 - (b-d)^2}, \quad (D13)$$

and

$$\sum_k \mathbf{v}_k^\dagger B(k) \mathbf{v}_k = \sum_k \left(\omega_3(k) \tilde{p}_{k,3}^\dagger \tilde{p}_{k,3} + \frac{\omega_3(k)}{2} \right), \quad (D14)$$

$$\omega_3 = 2\sqrt{a^2 - b^2}. \quad (D15)$$

The ground state energy is given as

$$\begin{aligned} E_{\text{GS}}^{\text{MF}} &= \sum_k \left(\frac{5}{2} \mu - \frac{3}{2} J_1 - \mu \bar{s}^2 + \frac{\omega_1(k) + \omega_2(k) + \omega_3(k)}{2} \right) \\ &= N_d \left(\frac{5}{2} \mu - \frac{3}{2} J_1 - \mu \bar{s}^2 + \sum_{l=1}^3 C_l E(X_l) \right), \\ C_1 &= \frac{1}{\pi} \left(|\epsilon_{p_1} - \mu| (|\epsilon_{p_1} - \mu| + |\lambda(1-\gamma)(-J_1 + 2J_2) \bar{s}^2|) \right)^{1/2}, \\ X_1 &= \left(\frac{2|\lambda(1-\gamma)(-J_1 + 2J_2) \bar{s}^2|}{|\epsilon_{p_1} - \mu| + |\lambda(1-\gamma)(-J_1 + 2J_2) \bar{s}^2|} \right)^{1/2}, \\ C_2 &= \frac{1}{\pi} \left(|\epsilon_{p_{-1}} - \mu| (|\epsilon_{p_{-1}} - \mu| + |\lambda(1+\gamma)(-J_1 + 2J_2) \bar{s}^2|) \right)^{1/2}, \\ X_2 &= \left(\frac{2|\lambda(1+\gamma)(-J_1 + 2J_2) \bar{s}^2|}{|\epsilon_{p_{-1}} - \mu| + |\lambda(1+\gamma)(-J_1 + 2J_2) \bar{s}^2|} \right)^{1/2}, \\ C_3 &= \frac{1}{\pi} \left(|\epsilon_{p_0} - \mu| (|\epsilon_{p_0} - \mu| + |\lambda(-J_1 + 2J_2) \bar{s}^2|) \right)^{1/2}, \\ X_3 &= \left(\frac{2|\lambda(-J_1 + 2J_2) \bar{s}^2|}{|\epsilon_{p_0} - \mu| + |\lambda(-J_1 + 2J_2) \bar{s}^2|} \right)^{1/2}, \end{aligned} \quad (D16)$$

where we use the complete elliptic integral of the second kind with $0 \leq m \leq 1$,

$$E(m) = \int_0^{\frac{\pi}{2}} \sqrt{1 - m^2 \sin^2 \theta} d\theta, \quad (D17)$$

We searched for the solutions (μ, \bar{s}^2) by numerically over the parameter space that gives $\omega_l \in \mathbb{R}$ for $\min_{\mu, \bar{s}^2} E_{\text{GS}}^{\text{MF}}$:

$$\begin{aligned} |\epsilon_{p_1} - \mu| &\geq |\lambda(1-\gamma)(-J_1 + 2J_2) \bar{s}^2|, \\ |\epsilon_{p_{-1}} - \mu| &\geq |\lambda(1+\gamma)(-J_1 + 2J_2) \bar{s}^2|, \\ |\epsilon_{p_0} - \mu| &\geq |\lambda(-J_1 + 2J_2) \bar{s}^2|, \\ 0 &\leq \bar{s}^2 \leq 1, \\ 0 &\leq \mu \leq 1. \end{aligned} \quad (D18)$$

- * saito-hidehiro722@g.ecc.u-tokyo.ac.jp
- ¹ P. Anderson, *Materials Research Bulletin* **8**, 153 (1973).
 - ² P. W. Anderson, *Science* **235**, 1196 (1987).
 - ³ Y. Zhou, K. Kanoda, and T.-K. Ng, *Rev. Mod. Phys.* **89**, 025003 (2017).
 - ⁴ A. Kitaev, *Annals of Physics* **321**, 2 (2006).
 - ⁵ G. Jackeli and G. Khaliullin, *Phys. Rev. Lett.* **102**, 017205 (2009).
 - ⁶ J. c. v. Chaloupka, G. Jackeli, and G. Khaliullin, *Phys. Rev. Lett.* **105**, 027204 (2010).
 - ⁷ J. G. Rau and M. J. P. Gingras, *Phys. Rev. B* **98**, 054408 (2018).
 - ⁸ J. G. Rau, E. K.-H. Lee, and H.-Y. Kee, *Annual Review of Condensed Matter Physics* **7**, 195 (2016).
 - ⁹ F. Pollmann, A. M. Turner, E. Berg, and M. Oshikawa, *Phys. Rev. B* **81**, 064439 (2010).
 - ¹⁰ S. Miyahara and K. Ueda, *Phys. Rev. Lett.* **82**, 3701 (1999).
 - ¹¹ T. Nomura, P. Corboz, A. Miyata, S. Zherlitsyn, Y. Ishii, Y. Kohama, Y. H. Matsuda, A. Ikeda, C. Zhong, H. Kageyama, and F. Mila, *Nature Communications* **14** (2023), 10.1038/s41467-023-39502-5.
 - ¹² K. Penc and A. M. Läuchli, “Spin Nematic Phases in Quantum Spin Systems,” in *Introduction to Frustrated Magnetism*, edited by C. Lacroix, P. Mendels, and F. Mila (Springer-Verlag Berlin Heidelberg, 2011) Chap. 13, p. 331.
 - ¹³ A. V. Chubukov, *Phys. Rev. B* **43**, 3337 (1991).
 - ¹⁴ K. Harada and N. Kawashima, *Phys. Rev. B* **65**, 052403 (2002).
 - ¹⁵ T. Hikihara, L. Kecke, T. Momoi, and A. Furusaki, *Phys. Rev. B* **78**, 144404 (2008).
 - ¹⁶ A. Läuchli, F. Mila, and K. Penc, *Phys. Rev. Lett.* **97**, 087205 (2006).
 - ¹⁷ Y. Shimizu, K. Miyagawa, K. Kanoda, M. Maesato, and G. Saito, *Phys. Rev. Lett.* **91**, 107001 (2003).
 - ¹⁸ P. Mendels and F. Bert, *Comptes Rendus. Physique* **17**, 455 (2015).
 - ¹⁹ M. R. Norman, *Rev. Mod. Phys.* **88**, 041002 (2016).
 - ²⁰ W. Lu, J. Tuchendler, M. von Ortenberg, and J. P. Renard, *Phys. Rev. Lett.* **67**, 3716 (1991).
 - ²¹ H. Kageyama, K. Yoshimura, R. Stern, N. V. Mushnikov, K. Onizuka, M. Kato, K. Kosuge, C. P. Slichter, T. Goto, and Y. Ueda, *Phys. Rev. Lett.* **82**, 3168 (1999).
 - ²² J. G. Rau, E. K.-H. Lee, and H.-Y. Kee, *Phys. Rev. Lett.* **112**, 077204 (2014).
 - ²³ W. Yang, A. Nocera, and I. Affleck, *Phys. Rev. Res.* **2**, 033268 (2020).
 - ²⁴ H. Saito, H. Nakai, and C. Hotta, *Journal of the Physical Society of Japan* **93**, 034701 (2024).
 - ²⁵ Y. Ohmagari, T. Onimaru, Y. Yamane, Y. Shimura, K. Umeo, T. Takabatake, H. Sato, N. Kikugawa, T. Terashima, H. T. Hirose, and S. Uji, *J. Phys. Soc. Jpn.* **89**, 093701 (2020).
 - ²⁶ F. Hori, K. Kinjo, S. Kitagawa, K. Ishida, S. Mizutani, R. Yamamoto, Y. Ohmagari, and T. Onimaru, *Commun. Mater.* **4** (2023), 10.1038/s43246-023-00381-4.
 - ²⁷ T. Hikihara, T. Momoi, A. Furusaki, and H. Kawamura, *Phys. Rev. B* **81**, 224433 (2010).
 - ²⁸ C. K. Majumdar and D. K. Ghosh, *Journal of Mathematical Physics* **10**, 1388 (1969).
 - ²⁹ C. Majumdar and D. Ghosh, *Journal of Mathematical Physics* **10**, 1399 (1969).
 - ³⁰ F. D. M. Haldane, *Phys. Rev. B* **25**, 4925 (1982).
 - ³¹ K. Okamoto and K. Nomura, *Physics Letters A* **169**, 433 (1992).
 - ³² S. Eggert, *Phys. Rev. B* **54**, R9612 (1996).
 - ³³ T. Hikihara, M. Kaburagi, and H. Kawamura, *Phys. Rev. B* **63**, 174430 (2001).
 - ³⁴ R. Bursill, G. A. Gehring, D. J. J. Farnell, J. B. Parkinson, T. Xiang, and C. Zeng, *Journal of Physics: Condensed Matter* **7**, 8605 (1995).
 - ³⁵ M. Kumar, A. Parvej, and Z. G. Soos, *Journal of Physics: Condensed Matter* **27**, 316001 (2015).
 - ³⁶ Z. G. Soos, A. Parvej, and M. Kumar, *Journal of Physics: Condensed Matter* **28**, 175603 (2016).
 - ³⁷ S. R. White and I. Affleck, *Phys. Rev. B* **54**, 9862 (1996).
 - ³⁸ C. Itoi and S. Qin, *Phys. Rev. B* **63**, 224423 (2001).
 - ³⁹ S. Furukawa, M. Sato, S. Onoda, and A. Furusaki, *Phys. Rev. B* **86**, 094417 (2012).
 - ⁴⁰ C. E. Agrapides, S.-L. Drechsler, J. van den Brink, and S. Nishimoto, *SciPost Phys.* **6**, 019 (2019).
 - ⁴¹ T. Hamada, J.-i. Kane, S.-i. Nakagawa, and Y. Natsume, *Journal of the Physical Society of Japan* **57**, 1891 (1988).
 - ⁴² R. D. Somma and A. A. Aligia, *Phys. Rev. B* **64**, 024410 (2001).
 - ⁴³ E. Plekhanov, A. Avella, and F. Mancini, *The European Physical Journal B* **77**, 381 (2010).
 - ⁴⁴ S. Hirata and K. Nomura, *Phys. Rev. B* **61**, 9453 (2000).
 - ⁴⁵ C. Gerhardt, K.-H. Mütter, and H. Kröger, *Phys. Rev. B* **57**, 11504 (1998).
 - ⁴⁶ R. Jafari and A. Langari, *Phys. Rev. B* **76**, 014412 (2007).
 - ⁴⁷ K. Okunishi and T. Tonegawa, *Journal of the Physical Society of Japan* **72**, 479 (2003).
 - ⁴⁸ K. Okunishi, *Journal of the Physical Society of Japan* **77**, 114004 (2008).
 - ⁴⁹ J. Sudan, A. Lüscher, and A. M. Läuchli, *Phys. Rev. B* **80**, 04402 (2009).
 - ⁵⁰ H. Saito and C. Hotta, *Phys. Rev. Lett.* **132**, 166701 (2024).
 - ⁵¹ H. Saito and C. Hotta, (2024), unpublished.
 - ⁵² S. R. White, *Phys. Rev. Lett.* **69**, 2863 (1992).
 - ⁵³ S. R. White, *Phys. Rev. B* **48**, 10345 (1993).
 - ⁵⁴ A. Gendiar, M. Daniška, Y. Lee, and T. Nishino, *Phys. Rev. A* **83**, 052118 (2011).
 - ⁵⁵ T. Hikihara and T. Nishino, *Phys. Rev. B* **83**, 060414 (2011).
 - ⁵⁶ I. Maruyama, H. Katsura, and T. Hikihara, *Phys. Rev. B* **84**, 165132 (2011).
 - ⁵⁷ H. Katsura, *Journal of Physics A: Mathematical and Theoretical* **44**, 252001 (2011).
 - ⁵⁸ C. Hotta and N. Shibata, *Phys. Rev. B* **86**, 041108 (2012).
 - ⁵⁹ C. Hotta, S. Nishimoto, and N. Shibata, *Phys. Rev. B* **87**, 115128 (2013).
 - ⁶⁰ N. Shibata and C. Hotta, *Phys. Rev. B* **84**, 115116 (2011).
 - ⁶¹ A. F. Andreev and I. A. Grishchuk, *Sov. Phys. JETP* **60**, 267 (1984), [*Zh. Eksp. Teor. Fiz.* **87**, 467 (1984)].
 - ⁶² M. Kawano and C. Hotta, *Phys. Rev. B* **107**, 045123 (2023).
 - ⁶³ R. Makuta and C. Hotta, *Phys. Rev. Res.* **6**, 023133 (2024).
 - ⁶⁴ M. Kawano and C. Hotta, *Phys. Rev. Res.* **4**, L012033 (2022).
 - ⁶⁵ M. Yamashita, S. Sugiura, A. Ueda, S. Dekura,

- T. Terashima, S. Uji, Y. Sunairi, H. Mori, E. I. Zhilyaeva, S. A. Torunova, R. N. Lyubovskaya, N. Drichko, and C. Hotta, *npj Quantum Materials* **6** (2021), 10.1038/s41535-021-00387-6.
- ⁶⁶ G. Vidal, *Phys. Rev. Lett.* **93**, 040502 (2004).
- ⁶⁷ F. B. Ramos, S. Eliëns, and R. G. Pereira, *Phys. Rev. B* **98**, 094431 (2018).
- ⁶⁸ T. A. Tóth, A. M. Läuchli, F. Mila, and K. Penc, *Phys. Rev. B* **85**, 140403 (2012).
- ⁶⁹ M. W. Haverkort, *Phys. Rev. Lett.* **105**, 167404 (2010).
- ⁷⁰ L. J. P. Ament, M. van Veenendaal, T. P. Devereaux, J. P. Hill, and J. van den Brink, *Rev. Mod. Phys.* **83**, 705 (2011).
- ⁷¹ P. D. Sacramento and V. R. Vieira, *Journal of Physics: Condensed Matter* **14**, 591 (2001).
- ⁷² S. Sachdev and R. N. Bhatt, *Phys. Rev. B* **41**, 9323 (1990).
- ⁷³ H. T. Ueda and K. Totsuka, *Phys. Rev. B* **76**, 214428 (2007).
- ⁷⁴ K. Totsuka, P. Lecheminant, and S. Capponi, *Physical Review B* **86** (2012), 10.1103/physrevb.86.014435.
- ⁷⁵ Y. Yokoyama and C. Hotta, *Physical Review B* **97** (2018), 10.1103/physrevb.97.180404.
- ⁷⁶ L. Gulay and I. Oleksyuk, *Journal of Alloys and Compounds* **402**, 89 (2005).
- ⁷⁷ H. Kaneshima, *Crystal structure and fluctuation of rare earth compounds, $RCuS_2$ (Dy-Lu)*, Master's thesis, Hiroshima University (2021).
- ⁷⁸ K. M. Ranjith, S. Luther, T. Reimann, B. Schmidt, P. Schlender, J. Sichelschmidt, H. Yasuoka, A. M. Strydom, Y. Skourski, J. Wosnitza, H. Kühne, T. Doert, and M. Baenitz, *Phys. Rev. B* **100**, 224417 (2019).
- ⁷⁹ A. O. Scheie, Y. Kamiya, H. Zhang, S. Lee, A. J. Woods, A. M. Omanakuttan, M. G. Gonzalez, B. Bernu, J. W. Villanova, J. Xing, Q. Huang, Q. Zhang, J. Ma, E. S. Choi, D. M. Pajerowski, H. Zhou, A. S. Sefat, S. Okamoto, T. Berlijn, L. Messio, R. Movshovich, C. D. Batista, and D. A. Tennant, arXiv preprint arXiv:2207.14785 (2023), arXiv:2207.14785 [cond-mat.str-el].
- ⁸⁰ T. Xie, A. A. Eberharter, J. Xing, S. Nishimoto, M. Brando, P. Khanenko, J. Sichelschmidt, A. A. Tur-rini, D. G. Mazzone, P. G. Naumov, L. D. Sanjeewa, N. Harrison, A. S. Sefat, B. Normand, A. M. Läuchli, A. Podlesnyak, and S. E. Nikitin, *npj Quantum Materials* **8** (2023), 10.1038/s41535-023-00580-9.
- ⁸¹ J. Xing, L. D. Sanjeewa, A. F. May, and A. S. Sefat, *APL Materials* **9**, 111104 (2021).
- ⁸² D. Yamamoto, G. Marmorini, and I. Danshita, *Phys. Rev. Lett.* **112**, 127203 (2014).
- ⁸³ T. Onimaru, (2024), private communications.
- ⁸⁴ M. E. Zhitomirsky and H. Tsunetsugu, *EPL (Europhysics Letters)* **92**, 37001 (2010).
- ⁸⁵ K. Penc, J.-B. Fouet, S. Miyahara, O. Tchernyshyov, and F. Mila, *Phys. Rev. Lett.* **99**, 117201 (2007).
- ⁸⁶ D. R. Nelson and M. E. Fisher, *Phys. Rev. B* **11**, 1030 (1975).